

Synthesis and Characterizations of LaMnO_3 Perovskite Powders Using Sol-Gel Method

Deniz ÇOBAN ÖZKAN (✉ deniz.coban@cbu.edu.tr)

Manisa Celal Bayar University: Manisa Celal Bayar Universitesi <https://orcid.org/0000-0002-8044-5952>

Ahmet Türk

Celal Bayar University: Manisa Celal Bayar Universitesi

Erdal Celik

Dokuz Eylül University: Dokuz Eylul Universitesi

Research Article

Keywords: Bandgap, Ferroelectric, Sol-gel, LaMnO_3 , Solar cells

Posted Date: February 12th, 2021

DOI: <https://doi.org/10.21203/rs.3.rs-217058/v1>

License:   This work is licensed under a Creative Commons Attribution 4.0 International License.

[Read Full License](#)

Abstract

The present research demonstrates the synthesis and characterization of LaMnO_3 perovskite powders using the sol-gel technique for dye-sensitive solar cell applications. With this respect, transparent solutions were prepared from La and Mn based precursors, distilled water and citric acid monohydrate. Ammonium hydroxide was incorporated into the La-Mn solution in order to neutralize/precipitate at 24°C for 1 hour in the air. The solution was allowed to evaporate on a hot plate device at 90°C in the air. The obtained solutions were dried at 90°C for 24 hours to form a xerogel structure, dried at 200°C for 2 hours and consequently annealed at 500 and 850°C for 2 hours in the air. Thermal, structural, microstructural, optical and magnetic properties of the powders were characterized through differential thermal analysis-thermogravimetry (DTA-TG), Fourier transform infrared (FTIR), X-ray diffraction (XRD), X-ray Photoelectron Spectroscopy (XPS), scanning electron microscopy (SEM), Malvern zeta sizer (PSD), UV-vis spectrometer and vibrating sample magnetometer (VSM). The obtained results indicate promise, especially the low band range, that LaMnO_3 powders can be used in dye-sensitized solar cells and can positively affect performance and efficiency.

1. Introduction

Lanthanum-based perovskite materials possess ostensible optical [1, 2], magnetic [3–5] and catalytic properties [6]. These materials have been extensively preferred in many areas such as catalysts [7–9], chemical sensors [10], solid oxide fuel cell electrodes [7], hydrogen storage [11], optoelectronic devices [12], solar cells [13], magnetic materials [14, 15] by virtue of stability, different oxidation states, flexible oxygen stoichiometry, power conversion efficiency and isomorphic substitution of metals in their structures [10, 16]. Foremost these applications, solar energy produced from perovskite-based solar cells is one of the most up-and-coming alternative energy sources on account of its relatively high energy conversion efficiency, low production cost, low production toxicity, ease of manufacture and flexibility [17].

Owing to their stability, suitable bandgap, a lower cost lanthanum-based perovskites such as lanthanum manganite (LaMnO_3), lanthanum orthoferrite (LaFeO_3), lanthanum nickel oxide (LaNiO_3) and lanthanum cobaltite (LaCoO_3) display power conversion efficiency and they became a great alternative for solar cell implementations [18–20]. Of the perovskite materials, LaMnO_3 notably possesses photovoltaic, photocatalytic and magnetic applications [20–22] on account of high stability at high temperature for aggressive medium [23] and narrower bandgap [24] features.

As a magnetic material, LaMnO_3 literally indicates gorgeous attributes in tandem with photovoltaic characteristics. It is an orthorhombic perovskite structure insulating antiferromagnetic material and its Néel temperature (T_N) is approximately 140 K. The magnetic manners of LaMnO_3 material are acquired from Mn^{3+} ($3d^4$,) cations super-exchange interactions inasmuch as the Mn^{3+} cations are located in an octahedral crystal field with six oxygen anions as MnO_6 form. There is a strong correlation betwixt the e_g

and t_{2g} orbitals' electron spins and this triggers the Jahn–Teller distortion of MnO_6 octahedra around Mn^{3+} ions. In addition to these, with the increase in the amount of oxygen, $(LaMnO_{3+x})$ structure can form more Mn^{4+} ions. It leads to ferromagnetic double-exchange interactions of $Mn^{3+}-Mn^{4+}$ pairs, and antiferromagnetic $Mn^{4+}-Mn^{4+}$ ones [25].

The efficiency of $LaMnO_3$ material relies on the synthesis techniques [26] such as solid-state reaction [27], combustion synthesis [28], hydrothermal synthesis [29], sonochemical synthesis [30], co-precipitation method [31], EDTA glycine process [32], core-shell [33], nanowires [34] and sol-gel [16, 35]. In recent years, studies on $LaMnO_3$ synthesis have been launched using different precursors and several synthesis techniques in order to be applied for alternative realms of use. To illustrate these, L. Phan et. al. [25] soundly scrutinized the magnetocaloric effect and critical behavior of Fe-doped $LaMnO_3$ so as to engender the $LaMn_{0.9}Fe_{0.1}O_3$ phase. In addition to these, T. Shou et. al. [9] reported the catalytic effect of Fe doped $LaMnO_3$. Y. Song et. al. [36] synthesized the $LaMnO_{3-\delta}$ including oxygen vacancy by making use of the method of molten salt. S. Priyatharshni et. al. [37] studied various morphologies of nanoscale $LaMnO_3$ structures which were synthesized with a facile hydrothermal process with stable calcination temperature. Q. Sun et. al. [15] synthesized $LaMnO_3$ thin films with post-annealing in the oxygen atmosphere to appraise the influence of the excess oxygen on the transport, structural and magnetic behaviors.

In our initial attempt [38], we reported synthesis and characterizations of sol-gel derived $LaFeO_3$ perovskite powder in view of its superior properties. In the previous work, the obtained results indicate that the $LaFeO_3$ powders possess the potential for photocatalytic applications notably in the continuously applicable and sustainable dye-sensitized solar cells as futuristic and innovative approaches. There is no universally enshrined $LaMnO_3$ synthesis due to the lack of any specific studies on sustainable dye sensitive solar cells in the literature. Moreover, no such organized search has been systematically studied to shed light on the influence of the structural, optical, particle size and magnetic properties of $LaMnO_3$ for two different synthesis temperatures. In this research, the fundamental goal is to logically comprehend the profound impacts of the annealing behaviors of $LaMnO_3$ perovskite powder and to specify the effect of structural, optical and magnetic features depending on the annealing temperature.

2. Experimental Procedure

2.1. Solution preparation

There exist four primary stages in preparing a solution, they are preparation and characterization of transparent solutions, neutralization/precipitation method, and xerogel production. Each of these steps is prominent for nanoscale particle synthesis, the nanoparticle size of the particles is a major criterion for

the next stages. Each process conducted in the synthesis of powders is comprehensively denoted in the flow chart of Fig. 1.

For the synthesis of pure LaMnO_3 powders, first, a transparent solution precisely should be prepared. As listed in Table 1, lanthanum (La) and manganese (Mn) based solution was prepared to carry out the syntheses of LaMnO_3 by making use of nitrate-based precursors which produces another compound. The precursors used in the synthesis are adjusted according to stoichiometric ratios. Distilled water (H_2O) and citric acid monohydrate ($\text{C}_6\text{H}_8\text{O}_7 \cdot \text{H}_2\text{O}$) were employed as the solvent and chelating agent (ligand) respectively. The role of this chelating agent in solution is a chemical compound whose structure allows two or more donor atoms (or sites) to bond to the same metal ion at the same time and forms one or more rings [39].

Table 1
Properties and amounts of precursor materials, solvent, chelating agents for La and Mn based solution (LMO).

Solution	Chemical products	Concentration
LMO	Lanthanum nitrate hexahydrate ($\text{La}(\text{NO}_3)_3 \cdot 6\text{H}_2\text{O}$)	5.413 g (0.0125 mole)
	Manganese (II) nitrate tetrahydrate ($\text{Mn}(\text{NO}_3)_2 \cdot 4\text{H}_2\text{O}$)	3.235 g (0.0125 mole)
	Citric acid monohydrate ($\text{HOC}(\text{COOH})(\text{CH}_2\text{COOH})_2 \cdot \text{H}_2\text{O}$)	5.253 g (0.0250 mole)
	Distilled water (H_2O)	50 ml
	Ammonium hydroxide (NH_4OH)	7 ml

15 ml of distilled water was used as a solvent and 0.0125 mole of La (lanthanum nitrate hexahydrate - $\text{La}(\text{NO}_3)_3 \cdot 6\text{H}_2\text{O}$, 99.99%, Merck) and 0.0125 mole of Mn (manganese (II) nitrate tetrahydrate - $\text{Mn}(\text{NO}_3)_2 \cdot 4\text{H}_2\text{O}$, 99.99%, Sigma) sources were separately dissolved and vigorously mixed together. As well, 0,025 mol of citric acid monohydrate ($\text{HOC}(\text{COOH})(\text{CH}_2\text{COOH})_2 \cdot \text{H}_2\text{O}$, 99.99%, Iso) was veraciously dissolved in distilled water (15 ml) and this mixture was subsequently put in the solution in order to effectuate stable complexes of metals, which prevents the precipitation of the salts of these metals and the subsequent homogenization of the system. The total water volume was accurately adjusted to 50 ml. The solution was then shuffled on a magnetic stirrer at room temperature for 1 hour in the air. Whole processes had no sooner completed than the solution was made clear, transparent and stable.

The turbidity and pH values of the transparent solution had to be measured for solution characterization. Prior to the precipitation process, the turbidity of the prepared solution was calculated via turbidimeter (VELP TB1) in the range of 0–1000 ntu (nephelometric turbidity unit). At this step, the La-Mn solution was the color pink. With a standard pH meter, the pH value of the solution was measured to guess its characteristics, it was found that this value of the solution was below 1, which strongly represents an acidic character.

In the case of the neutralization/precipitation process, ammonium hydroxide (NH_4OH , $\geq 99.99\%$, Merc) was involved in the generation of hydroxide ions in this solution, boosting the pH to the point in which oxides were formed. NH_4OH was attentively incorporated into the La-Mn solution in a controlled manner with dropper control and checked with pH meter and pH-indicator strips. After adding 7 ml of NH_4OH , the pH value was measured as neutral (7) and the obtained solution was smartly stirred to neutralize/precipitate at 24°C for 1 hour in air. The color of the La-Mn solution was milky white. The solution was allowed to evaporate for 24 hours on a hot plate device at 90°C in air after the stirring procedure. This was followed by the production of xerogel powder, by acquiring an atomic mixture in the final product before drying and high-temperature annealing.

2.2. Heat treatment

In view of the fact that, in heat treatment, drying is a mass transfer process that comprises the removal of water or other solvents from solid, semi-solid and liquid by evaporation, structure features can be obtained by controlling the diffusion rate and cooling rate within the microstructure by heat treatment. In the realm of this, heat treating is frequently used to alter the structural, microstructural, mechanical, optical, magnetic and solar cell efficiencies of the materials. For proper heat treatment, it requires precise control over temperature, rate of ascent to this temperature, holding time at this temperature and cooling rate. The main objective of process annealing is to produce a uniform microstructure and improve properties, as mentioned in literature [40–42]

The drying and annealing processes required for the growth of the LaMnO_3 powder are posed in Fig. 2 (see for more details). Our material, which comes in the form of xerogel on the hot plate is divided into two and both are dried at 200°C for 2 hours in the air. Subsequently, with a heating rate of $5^\circ\text{C}/\text{minute}$, the samples are heated up to 500 and 850°C and kept at these temperatures for 2 hours. Hereafter, they were left to cool down in the electric furnace. In accordance with the DTA-TG results presented in-dept in the ensuing sections, the heating regimes of the drying and annealing processes were sensibly simulated.

2.3. Characterizations

Thermal analyses of xerogel kept on a hot plate at 90°C for 24 hours and ceramic powder heated at 500°C for 2 hours were conducted by means of DTG-60H Model Differential Thermal Analysis-Thermogravimetric Analysis (DTA-TGA) machine in an air environment at $5^\circ\text{C}/\text{min}$ heating rate. With these analyses, an optimum heat treatment procedure was gained for drying, heat treatment and annealing regimes as well as obtaining decomposition and phase formation.

Fourier Transform Infrared (FTIR) spectra of La-Mn based xerogel and powders were recorded to cast light on the bonds in their structures through an ATR attached FTIR spectrometer (Thermo Scientific Nicolet IS10).

X-ray Diffraction (XRD) patterns of the ceramic powders were employed to extensively clarify their crystal structures and temperature dependent phase transformations at the temperature between 500°C and

850 °C by way of a Thermo-Scientific, ARL-K_α diffractometer with working settings of 45 kV – 44 mA and CuK_α irradiation (wavelength, $\lambda = 0.15418$ nm).

X-ray Photoelectron Spectroscopy (XPS, Thermo Scientific Al K_α) and monochromatic Al-K_α (1486.7eV) X-ray source with 400 nm diameter beam size was exploited to define the elemental composition and surface chemistry of the powder specimens synthesized at 500°C and 850°C. The curve fitting program supplied by the Product Company (ThermoAantageV5.65 programs) was used to specify binding energies and deconvoluted spectra.

In order to observe the surface morphology of La-Mn based xerogel and ceramic powders, Zeiss Sigma 300 VP model Scanning Electron Microscope (SEM) equipment operating at 8–10 kV acceleration voltage was employed at 20 kV.

In order to measure the average particle sizes and particle size distributions of LaMnO₃ powders, the Malvern Zeta Sizer ZS90 (PSD) was utilized. The powders must be dispersed in a liquid for particle size measurement and distilled water is used as the liquid at room temperature. To determine the particle size in the device, the type of the used liquid and the refractive indices (2.50) of LaMnO₃ powders must be entered in its program [43, 44].

Optical measurements of the ceramic samples were identified with a UV Vis spectrophotometer (Thermo Scientific Evolution 600) with diffused reflectance apparatus in the wavelength range of 300–850 nm.

Magnetic features of the powders were found through a Dexion Magnet-Vibrating Sample Magnetometer (NanoMagnetic Instruments Inc. VSM). The saturated magnetization (M_s), remanence magnetization (M_r) and coercive force (H_c) values of LaMnO₃ powders annealed at 500 °C and 850 °C were determined at 25 °C in air with this system.

3. Results And Discussion

3.1. Solution properties

In the sol-gel synthesis, two measurements are carried out in the solution step to determine whether the solution is prepared correctly and whether it can pose the desired properties. To be able to easily make sense of solution characteristics, one must have full knowledge of turbidity and acidic-basic manners. In this strict sense, these are measurements of turbidity and pH values determined bounding up with the precursors, solvent and chelating agents. The turbidity of the solutions is measured in NTU (Nephelometric Turbidity Units). This value, which is between 0 and 1000 NTU, approaches 0 NTU in case the precursors are entirely dissolved in the solution and a homogeneous solution is obtained and approaches 1000 NTU unless it is dissolved properly [39]. As might be expected, the turbidity value measured before the ammonium hydroxide addition is 0.79 NTU, which means that the precursors

decently dissolve in the solvent and are appropriate for the production of the stoichiometric perovskite structure.

As we elaborately explained in our former study [38], the acidic and basic features of the prepared solution reasonably give paramount hints for hydrolysis and condensation processes. Taking into consideration of the pH values in the solution phase, it is well reckoned that strong acidic pH (2–3) values entail slow gelation, which is ideal for the formation of an expanded network, while basic pH (8–9) values trigger swift gelation, which is optimum for the formation of smaller aggregates. Keep in mind that the desired neutral pH value of the solution is readily adjusted by putting in ammonium hydroxide (NH_4OH) so as to acquire the intended perovskite structure, as reported in Refs. [38, 45–47].

3.2. Thermal behavior

Due to the fact that thermal analysis is a sort of simulation of the actual conditions of the heat treatment regimes for xerogels and powders, it is greatly benefited from DTA-TGA as a thermal analysis technique. In the analysis, it aims to obtain the proper heating regime and annealing temperature for the whole process. The La-Mn based xerogel dried at room temperature and the powder heat-treated at 500 °C is analyzed at atmospheric conditions at a temperature range of 25–990 °C at a heating rate of 5 °C/min. The thermal analysis gives information about changes in material properties as a function of temperature. While DTA registers changes in the material where no mass loss occurs, e.g. crystal structure changes, melting, glass transition, etc, TGA only measures changes caused by mass loss.

DTA-TGA curves of the La-Mn-based xerogel sample dried at 90 °C are depicted in Fig. 3. Once the curves are examined, there are small endothermic peaks at nearly 100 °C, which is interrelated to the removal of physically adsorbed H_2O from the xerogel structure [48] coming from precursors, citric acid monohydrate and distilled water (see Table 1). It is also explicit that exothermic peaks range from 180 °C to 280 °C are existed and they are concerned to thermal combustion of organic groups [49] originating from citric acid monohydrate, and La-Mn xerogel's large peak at 262 °C can be defined as by the alteration of the chemical precursor type. The weeny peak at 400 °C reflects thermal decomposition of the salt group ($(\text{NO}_3)^{-1}$) stemming from lanthanum nitrate hexahydrate and manganese (II) nitrate tetrahydrate. As is to be expected, the small peaks in the temperature range of 430 °C and 550 °C are the same as the oxidation process and it is figured out that the oxide forms commence crystallizing at 430 °C in La and Mn based xerogel. It is an undeniable fact that oxide structures formed at these temperatures are like single oxides such as La_2O_3 and MnO_2 , which we do not want, or non-stoichiometric perovskite oxides. In order to eliminate these undesired oxide structures, temperatures above 500 °C were raised and pure perovskite phase peaks containing LaMnO_3 were observed. Even if large changes in the curve cannot be observed due to the low mass of the DTA-TGA sample, a change in slope at approximately 600–720 °C and slope curves at about 800–850 °C were determined. From the TGA curves in Fig. 3, it can be obviously seen that the weight loss value of La-Mn xerogel is 17.16% and that a steep decline of this weight loss occurs as an exothermic reaction at temperatures between 180 °C and 280 °C. After 280 °C, the weight loss

Loading [MathJax]/jax/output/CommonHTML/jax.js 00 °C and is over.

DTA-TGA analysis of the LaMnO_3 ceramic powder sample, which was subjected to air heat treatment at 500°C for 2 hours, was performed to reveal the topotactic and phase transformations after 500°C more clearly (Fig. 4). As mentioned elsewhere [50, 51], after a gel dries, it is generally heated at much higher temperatures than drying, so that conversions to more stable phases can occur. Note that a crystalline transition phase is usually produced by heat treatments at a temperature between 100°C and 1000°C . To put it another way, while these phases are generally produced at high temperatures, new thermodynamically unstable phases are formed by topotactic transformation at intermediate temperatures. As these intermediate temperatures are headed, a series of topotactic transformations are observed and gradually more stable phases emerge until the most stable thermodynamic phase is fully formed. Intermediate stages are called transitional phases. Topotactic transformation sequences and formed intermediate phases hinge on the initial gel structure and accordingly the chemical recipe used in sol-gel processing. When the processing temperature is increased after 500°C , the topotactic reactions begin in the temperature range of 540°C and 680°C . In detail, the first topotactic reactions engender at $513\text{--}516\text{--}520^\circ\text{C}$ and $540\text{--}560\text{--}580^\circ\text{C}$, respectively, while the second topotactic reactions take place at $620\text{--}650^\circ\text{C}$, $623\text{--}660^\circ\text{C}$, $640\text{--}680^\circ\text{C}$ respectively. The most appealing aspect in the determination of heat treatment profile is that nucleation and growth of fully stoichiometric perovskite structures occur in the temperature ranges of $752\text{--}848^\circ\text{C}$, $756\text{--}877^\circ\text{C}$ and $766\text{--}900^\circ\text{C}$.

Pursuant to the DTA-TGA results, the heat treatment regime can be obtained to be implemented for La-Mn based ceramic specimens by using the exothermic and endothermic reactions. By taking into consideration these reactions in the temperature range from 24°C to 900°C , evaporation/solvent removal at 100°C , combustion/decomposition at $150\text{--}430^\circ\text{C}$, oxidation/crystallization at $400\text{--}500^\circ\text{C}$, topotactic reactions at $500\text{--}650^\circ\text{C}$ and phase formation at $650\text{--}850^\circ\text{C}$ can be easily determined from DTA-TGA results. DTA-TGA analysis simulates the heat treatment process in the electric furnace from 24 to 1000°C . Based on these results, the heat treatment of the xerogel sample dried at 90°C for 24 hours is divided into two processes. Both processes are heated in the electric furnace at a rate of $5^\circ\text{C}/\text{min}$ in air. The first process is drying one, which was performed at 200°C for 2 hours and the second process is annealing one, which was carried out at 500°C and 850°C for 2 hours. The samples were then left to cool down in the furnace environment. Using the temperatures in the exothermic and endothermic reactions in the DTA-TG results, the optimum heating regimes of the drying and annealing processes were precisely determined.

3.3. FTIR analysis

To gain more insight into the chemical structures of La-Mn based materials in the temperature range of 25°C and 900°C , FTIR analysis was carried out in detail. FTIR spectra of LaMnO_3 at heat treated at 90°C , 500°C and 850°C are illustrated in Fig. 5. In the form of xerogel dried at 90°C , antisymmetric stretching and strong antisymmetric in-plane bending of NO_3^- in nitrate groups are noticed approximately at $840\text{--}880\text{ cm}^{-1}$ [52]. At $1360\text{--}1480\text{ cm}^{-1}$ bands pertinent to the vibration mode of the carboxylic group structure and other phases in the co-precipitation sample exists,

as explained in Ref. [53–55]. In the range of $3200 - 2800 \text{ cm}^{-1}$ symmetrical and asymmetrical expansions, O-H expansions, N-H expansions and vibrations are determined [56]. The hydroxyl (OH) group's peak at 1626 cm^{-1} [52] and a peak at 3214 cm^{-1} appertains the N-H groups. It is apparent that after the annealing processes, these bands are eliminated from the structure. Note that after the annealing process, FTIR spectra of the samples at 500 and $850 \text{ }^\circ\text{C}$ denotes the existence of M-O bonds (M = La and Mn) in different sites. It is a remarkable result that, in the range of $400 - 1000 \text{ cm}^{-1}$, two bands are found for perovskite structures. The higher one at $\sim 600 \text{ cm}^{-1}$ represents La-O and Mn-O stretching vibrations corresponding to octahedral LaO_6 and MnO_6 groups and the lower one at $\sim 400 \text{ cm}^{-1}$ represents La-O-La-O and Mn-O-Mn deformation vibrations [57]. In Fig. 5, the clearest peak is at 604 cm^{-1} for both powders and belongs to the vibration of the octagonal MnO_6 in the structure ABO_3 [5, 7, 8] and at 3609 cm^{-1} there is another peak which belongs to La-O in La_2O_3 [58]. The La_2O_3 peak is obviously observed in the gel form but after the annealing process, it is disappearing in that lanthanum is made a bond with Mn in the structures.

3.4. Phase analysis

XRD is a powerful non-destructive technique so as to characterize structures, phases, crystal orientations, and structural parameters of crystalline materials. As given in Fig. 6, XRD analysis was used to be identified the phase and crystal structures of the LaMnO_3 powders annealed at $500 \text{ }^\circ\text{C}$ and $850 \text{ }^\circ\text{C}$. In the XRD analysis, it is also obvious that the LaMnO_3 phase was successfully obtained in LaMnO_3 powder samples at both temperatures. Nonetheless, even though it can be emphasized that LaMnO_3 synthesis is possible at both temperatures once the peaks in the XRD analysis are compared, the intensity of the peaks and the noise in the graph differ. In the production of pure perovskite, any crystalline impurities like La_2O_3 or MnO_2 are not requested after annealing processes. Generally speaking, increasing the annealing temperature comes up as a result of the elimination of the unwanted phases with the growth of perovskite structure. This issue strongly backs up DTA-TGA and FTIR findings.

XRD results present that LaMnO_3 is apparently formed in the orthorhombically distorted perovskite structure, consisting of oxygen octahedra with a central Mn atom. This is evident that the characteristic diffraction peaks of LaMnO_3 powder with the orthorhombically distorted perovskite structure remarked good crystallinity (JCPDS Card No. 50–0298). In the LaMnO_3 sample, the main characteristic reflexes are located at 2θ of 23.0° , 32.8° , 40.2° , 47.0° , 52.6° , 58.2° , 68.7° , and 77.9° being indexed to the (012), (110), (202), (024), (122), (214), (208) and (134) diffraction planes, respectively.

Making use of the XRD data, it is possible to estimate the crystalline size of the materials. For this, the diffraction peaks were employed with the Scherrer Equation to guest the crystallite sizes of LaMnO_3 powders.

$$(D=K\lambda/\beta\cos\theta), \quad (1)$$

In this equation, the shape factor (K) is 0.94, $\lambda = 1.5418 \text{ \AA}$, β is the full width at half maximum (FWHM) (radians), and θ is Bragg's angle (radians) [59]. The XRD data of the powders are calculated for crystallite sizes for all diffraction peaks, as shown in Table 2. As might be expected, according to estimations, the average crystallite sizes were determined to be 20.58 nm in 500 °C, and 24.79 nm in 850 °C for LaMnO₃. Upon examining these data, it is perceived that when the annealing temperature rises from 500 °C to 850 °C, the grain growth takes place in ceramic powders, and in its parallel, this boosts the crystallite sizes.

Table 2
Peak positions, FWHMs, and crystallites sizes of LaMnO₃ annealed at 500°C and 850°C

	Peak position 2θ (°)	FWHM B _{size} (°)	L (nm)	Ave. L (nm)		Peak position 2θ (°)	FWHM B _{size} (°)	L (nm)	Ave. L (nm)
LMO 500 °C	22,92	0,65809	12,32	20,58	LMO 850 °C	23,32	0,30173	26,89	24,79
	32,58	0,33324	24,84			32,88	0,50852	16,29	
	40,24	0,31331	27,01			40,48	0,425	19,93	
	46,76	0,74123	11,68			47,12	0,35429	24,47	
	57,92	0,53836	16,87			58,34	0,45001	20,22	
	68	0,34288	27,95			68,34	0,22335	43,00	
	77,44	0,43599	23,36			77,96	0,45001	22,71	

3.5. Elemental analysis

Upon setting out with the aim to present all details of elemental analysis, XPS analysis is utilized in specifying the valence states of elements for LaMnO₃ samples as a distinctive quality. Survey scans and high-resolution XPS spectra are illustrated in Fig. 7 and Table 3. It is a very dear outcome that valence states of manganese and lanthanum in LaMnO₃ are reported to be La-3d₅ and Mn-2p for powders at both synthesis temperatures. In Fig. 7, XPS results of both LaMnO₃ powders synthesized at 500 and 850 °C are presented. Whilst Fig. 7a exhibits the general survey scan data, Figs. 7b and 7c depict the La-3d and Mn-2p core-level XPS spectra respectively. The C1s peak in the XRD survey scan comes from the CO₂ from the air and the carbon tape used during analysis, and it gives the C1s signal at 284.84 eV and O-1s peaks are determined at 530 eV in both [60, 61]. In Fig. 7b, namely La-3d XPS spectrum, there are four obvious peaks and these are 834 and 838 eV for La-3d_{5/2} and 851 and 855 eV for La-3d_{3/2} binding energy of and its satellite peak [61, 62]. La-3d peaks in the XPS spectrum indicate the presence of the

La³⁺ oxidation state. In Fig. 7c, there are two signals in 642 and 654 eV and they represent Mn2p_{3/2} and Mn2p_{1/2}. Mn-2p peaks in the XPS spectrum indicate the presence of the Mn²⁺ oxidation state.

Table 3
Elemental ID and quantification for LaMnO₃ annealed at 500°C and 850°C

	<i>Name</i>	<i>Peak BE</i>	<i>FWHM (eV)</i>	<i>Area (P) CPS (eV)</i>	<i>Weight (%)</i>	<i>Q</i>
LaMnO ₃ 850°	La3d5	835.52	3.09	1236378	57.11	1
	O1s	530.98	3.38	410936.52	18.82	1
	Mn2p	643.12	3.91	383637.74	15.45	1
	C1s	286.04	2.82	103696	8.63	1
LaMnO ₃ 500°	La3d5	834.87	3.5	57107.6	44.92	1
	O1s	530.15	3.46	28376.27	22.13	1
	Mn2p	642.34	3.55	26408.48	18.11	1
	C1s	285.09	2.22	10467.47	14.84	1

In a general overview of XPS, lanthanum peaks have the same amplitude and amplitude in both regions and the same amplitude and value in manganese peaks. When XPS analyses are compared with FTIR and XRD results, it is seen that there is a good agreement. To be quite frank, in these results, it can be expressed that the LaMnO₃ ceramic perovskite structure was successfully synthesized at both temperatures.

3.6. Microstructure

SEM observations are concerned with the question of how heat treatment temperatures such as 90 °C, 500 °C and 850°C can be altered the profound impacts on microstructures of LaMnO₃ powders in the sol-gel process. Due to this reason, SEM images were employed to examine the surface morphology of xerogel and ceramic perovskite powder materials and to approximately determine particle sizes. As is known, the surface morphology of LaMnO₃ powder materials rests on sol-gel parameters such as drying and annealing conditions. SEM micrographs in Figs. 8, 9 and 10 respectively refer to LaMnO₃ xerogel and ceramic powder materials derived from sol-gel solutions and subsequently heat treated at 90 °C, 500 °C and 850°C. The microstructures of La-Mn based xerogel dried at 90 °C are shown in Fig. 8a. The xerogel powder has an irregular shape. On the grounds of the charge of many physical specifications like rheological properties and water-holding, the xerogel powders can schematically be separated into fine-stranded and aggregated or particulate gels [63]. Once Fig. 8b is thoroughly examined, it is seen that the sizes of the particles are between ~5 µm and 40 µm. In addition to these, it can be noted that there are

approximately 5 µm and 25 µm (see Fig. 8 for details). It is well-

known that gel networks have water-holding properties and with the increase in the network structure, the water-holding properties increases [64, 65].

As to the surface morphologies of LaMnO_3 ceramic powder annealed at $500\text{ }^\circ\text{C}$, as denoted in Fig. 9, it can be noticed that the powder has nearly round-shaped small-sized grains. When the average particle sizes of the powders are measured, they are in the range of 50-1500 nm, and these sizes are agreed by the Ref [13]. Notwithstanding these grains, there also is an agglomeration process during sol-gel synthesis and the agglomerated particle size of the fine powders is in the range of 20–100 μm [66]. Even the presence of agglomerations of very fine particles smaller than 100 nm can be intuited in the images, because of not having a surface protective layer. However, the particle shapes are not well defined and the powders contain large and small pores.

As far as LaMnO_3 ceramic powder annealed at $850\text{ }^\circ\text{C}$ is concerned, its surface morphologies can be clearly seen in Fig. 10. In a contextual sense with the powder sample annealed at $500\text{ }^\circ\text{C}$, the LaMnO_3 ceramic powder annealed at $850\text{ }^\circ\text{C}$ generally exhibits similar characteristic behaviors except for its particle size. It is clear in Fig. 10 that the powder has fine submicron and nano-scaled particles with nearly round shapes. Upon measuring the average particle sizes, it is found to be in the range of 50–250 nm, which is a good result in favor of dye-synthesized solar cell application. We have a good agreement about the sizes of the powders in Ref [16]. In the fundamental finding as to its particle size, such an essential distinction is annealing temperature in sol-gel processing. As indicated in these SEM images, the increase in the annealing temperature gradually reduces the porosity and agglomeration. It can be implied that though powders annealed at $850\text{ }^\circ\text{C}$ are spherical, powders annealed at $500\text{ }^\circ\text{C}$ possess a sphere-like structure. It is believed that the particle size and shape of LaMnO_3 ceramic powder strongly influence the microstructure and power performance of dye-synthesized nanocomposite.

3.7. Particle size analysis

In order to compare and detail the particle sizes observed in the SEM images, the particle size analysis was evaluated by using the particle size distribution of the powders. These perovskite powders are planned to be used in dye-sensitive solar cell applications, and it is thought that the low particle size in these applications not only stabilizes the cell more but also increases the power conversion efficiency. The particle sizes and distributions of both LaMnO_3 ceramic powders (annealed at $500\text{ }^\circ\text{C}$ and $850\text{ }^\circ\text{C}$) prepared by dispersing in pure water were determined using Malvern zeta sizer (Fig. 11). It is especially indicated that these results are consistent with the SEM micrographs in Figs. 9–10.

The particle size values of the sol-gel derived LaMnO_3 ceramic powders annealed at $500\text{ }^\circ\text{C}$ were found to be approximately 571 nm (the range of 60-1400 nm) and that of at $850\text{ }^\circ\text{C}$ were determined to be as nearly 305 nm (in the range of 58-1200 nm). In terms of these results, it can be apparently accentuated that particle sizes decrease as the annealing temperature increases. Depending on these outcomes, the particle size analysis confirms XRD and SEM results.

It is especially indicated in Fig. 11 that small and large particles are described with two obvious peaks. In this case, these particles are dispersed in a liquid (water) and randomly moving, with the help of the dynamic light scattering mechanism these are determined. In this mechanism, the movement speed of the particles is applied to determine the particle size, and this movement continues. Therefore, if we take two 'peaks' of the powder the amount of motion of the sample particles separated by a short time interval is determined and therefore their size can be calculated. The reason why the particles in the sample are calculated as large is that there is a minimal particle movement between the two 'peaks'; Likewise, the small size removal of particles in the sample may also result from a large amount of movement between the two 'peaks'. [67]. In the zeta sizer machine, light scattering is a very convenient method for identifying single particles and aggregates thanks to its sensitivity to larger particles.

3.7. Optical properties

Why do not we focus our attention on the optical properties of LaMnO₃ powders? The LaMnO₃ powders we synthesized are aimed to be used in dye-sensitive solar cell applications. Therefore their optical behaviors have a critical place in this study. With UV-Vis spectroscopy used in determining optical properties, reflectance and transmission graphs depending on wavelength were obtained, as indicated in Figs. 12 and 13. The UV-Vis absorption edge is directly pertaining to the bandgap energy of the material (Fig. 14), and this bandgap directly affects the power conversion efficiency in solar cell applications.

Transmittance values in 320 nm and 800 nm wavelength range of pure LaMnO₃ powders annealed at 500 °C and 850 °C are demonstrated in Fig. 12 and reflectance values are portrayed in Fig. 13. Once the transmittance wavelength curve is examined, it is seen that the LaMnO₃ transmittance higher than about 90% for both annealing temperatures. Upon examining the reflection wavelength curve, a reflection of less than 5% is observed for pure LaMnO₃ between 350 nm and 500 nm, and this reflection rate plummets to 20% in the range of 320 nm to 350 nm and stabilizes up to 800 nm. When we assess these two curves in general, LaMnO₃ is a pertinent candidate for dye-sensitive solar cell applications.

Owing to the increase in crystallite size associated with higher densification of powders, there has been an increase in its transmittance through wavelengths [68]. These changes pertain to the electronic transition between the valance and conduction bands which are relevant to samples' optical bandgaps [69, 70]. Using the optical measurements of LaMnO₃ in the Kubelka-Munk (K-M) function, the bandgap in both synthesis temperatures was calculated using the graphs given in Fig. 14 [71]. This Kubelka-Munk (K-M) function method is based on the transformation of the diffuse reflectance through the following relation;

$$F(R) = \frac{\alpha}{S} = \frac{(1-R)^2}{2R} \quad (2)$$

In this formulation Kubelka-Munk function is “ $F(R)$ ”, the molar absorption coefficient is α , the scattering factor is S and the reflectance of the material is R . UV–vis diffuse reflectance measurements are exploited to predict the bandgap (E_g) energy. From a plot of $(F(R).hv)^2$ vs. hv , the bandgap energy can be determined by extrapolating the slope to $F(R) \rightarrow 0$ [72–75] and concisely summarized in Table 4 using the results of Fig. 14. According to Fig. 14, band gap values (E_g) were found as 1.27 eV for both temperatures. It is important to express here that as the band gaps of LaMnO_3 obtained by different production techniques in different studies were around 2.50 eV [3, 37, 76], in our synthesis, the bandgap of both of our LaMnO_3 powders was found to be 1.27 eV. When these optical results are taken into consideration, it can be discerned that LaMnO_3 powders prepared by the sol-gel method possess a very low bandgap value and this makes the LaMnO_3 structure promising for solar cell applications.

Table 4
The bandgap (E_g) energy of LaMnO_3 annealed at 500°C and 850°C

Materials	Temperature (°C)	Bandgap (E_g)
LaMnO_3	500	1.27 eV
LaMnO_3	850	1.27 eV

3.8. Magnetic properties

A vibrating sample magnetometer (VSM) was used to investigate the magnetic properties of LaMnO_3 materials annealed at 500 °C and 850 °C, magnetic hysteresis (M - H) cycles were acquired for both powders and the change of magnetic properties depending on the synthesis temperature is represented in Fig. 15 and Table 5. Sizes, sample shapes, crystallinities, magnetization directions, synthesis methods are the critical effects on magnetic properties e.g. magnetization, remanence and coercivity.

Table 5
The magnetic properties of LaMnO_3 powders annealed at 500°C and 850°C.

Sample name	Temperature (°C)	M_s (emu/g)	M_r (emu/g)	H_c (Oe)
LaMnO_3	500	0.96	0.1	82.96
LaMnO_3	850	1.69	0.1	82.95

Although lanthanum and manganese demonstrate paramagnetic properties [6, 77], magnetic hysteresis loops for two different annealing temperatures of LaMnO_3 in Fig. 15 denote soft ferromagnetic properties. In Table 5, remanent magnetization (M_r) and coercivity (H_c) values of both powders were found to be approximately the same value, 0.1 emu/g and 82.95 Oe, respectively, despite them, saturation magnetization (M_s) value was obtained 0,96 emu/g for 500 °C and 1,69 emu/g for 850 °C. In spite of the

fact that the remanent magnetization (M_r) and coercivity (H_c) values are independent of the synthesis temperature, also an increase in synthesis temperature increases the permanent magnetization values of LaMnO_3 . In other words, the increase in the annealing temperature in the synthesis causes the magnetic properties to increase likewise [78–81]. Considering that all the properties of the powders we obtain are the same except the synthesis temperature and also the particle sizes. It can be pointed out that the difference in the saturation magnetization (M_s) value is due to the difference in particle size.

The most striking feature is that the average particle sizes of LaMnO_3 powders are higher at 500 °C than that of 850 °C, whereas the magnetic saturation (M) values are higher at 850 °C than that of 500 °C. In general, for LaMnO_3 magnetic saturation increases by virtue of the decrease in the particle size, the change in the density of the particle and the decrease in the possible difference in the magnetic effect on the particle surface and volume.

4. Conclusion

To sum up, LaMnO_3 perovskite powders with orthorhombically distorted perovskite structure were successfully synthesized by using the sol-gel method at synthesis temperatures of 500 °C and 850 °C in the hope of being used in dye sensitive solar cell applications. We draw attention to the results of this research as follows:

1. By DTA-TGA analysis, the heat treatment regime from 24°C to 900 °C was determined to implement for La and Mn based xerogel and ceramic samples using exothermic and endothermic phenomena such as evaporation/solvent removal at 100 °C, combustion/decomposition at 150-430 °C, oxidation/crystallization at 400-500 °C, topotactic reactions at 500-650 °C and phase formation at 650-850 °C.
2. In FTIR analysis, bands at 604 cm^{-1} correspond to octagonal MnO_6 's strong Mn-O bond vibration, bands at 3609 cm^{-1} correspond to La_2O_3 's La-O bond. In the La-Mn-based gel, a La_2O_3 peak is seen but in the wake of the heat treatment process, it is disappearing because lanthanum makes a bond with manganese in the LaMnO_3 .
3. In XRD analysis, LaMnO_3 powder's purer single-phase can be seen in the sample annealed at 850 °C compared to annealed at 500 °C. The crystallite sizes of both powders are estimated as 20.58 nm for 500 °C and 24.79 nm for 850 °C.
4. According to survey scan XPS spectra and high-resolution XPS spectra, both LaMnO_3 samples have La-3d5 and Mn-2p valance states.
5. SEM images of the LaMnO_3 powder heat-treated at 500 °C are small grains with irregular shapes, but the powders annealed at 850 °C have very fine submicron and nanoscale particles of more spherical shape. The particle sizes of the sample annealed at 800 °C were determined to be in the range of 50-250 nm.

6. The average particle size of the powders was 571 nm for 500 °C and 305 nm for 850 °C. Particle sizes abate with increasing annealing temperature.
7. The bandgap value of LaMnO₃ powder was found to be 1.27 eV for both annealing temperatures. In this case, the bandgap of the LaMnO₃ powders is independent of the processing temperature.
8. VSM analysis revealed that LaMnO₃ has soft ferromagnetic features, even though La and Mn are paramagnetic materials. Even though the remanent magnetization (M_r) and coercivity (H_c) values are independent of the synthesis temperature, also increase in annealing temperature increases the permanent magnetization values of LaMnO₃. For LaMnO₃ magnetic saturation increases on account of the decrease in the particle size, the amendment in the density of the particle and the decrease in the possible difference in the magnetic effect on the particle surface and volume.
9. In general, these results point out that LaMnO₃ perovskite powders have a potential for photocatalytic applications as futuristic and innovative approaches, notably in continuously applicable and sustainable dye-sensitized solar cells.

Declarations

Acknowledgments

This research has been supported by Manisa Celal Bayar University Scientific Research Projects Coordination Unit. Project Number: 2018-049, Dokuz Eylul University Center of Fabrication and Application of Electronic Materials.

Conflict of Interest

The authors declare that they have no known competing financial interests or personal relationships that could have appeared to influence the work reported in this paper

References

- [1] S. Gong, B.G. Liu, Electronic energy gaps and optical properties of LaMnO₃, Phys. Lett. Sect. A Gen. At. Solid State Phys. 375 (2011) 1477–1480. <https://doi.org/10.1016/j.physleta.2011.02.027>.
- [2] C. Ma, W. Ren, L. Wang, J. Xu, A. Chang, L. Bian, Structural, optical, and electrical properties of (Mn_{1.56}Co_{0.96}Ni_{0.48}O₄)_{1-x}(LaMnO₃)_x composite thin films, J. Eur. Ceram. Soc. 36 (2016) 4059–4064. <https://doi.org/10.1016/j.jeurceramsoc.2016.06.019>.
- [3] T. Ha, T. Huong, H. Nam, N. Hai, C. Viet, Results in Physics Sr doped LaMnO₃ nanoparticles prepared by microwave combustion method: A recyclable visible light photocatalyst, Results Phys. 19 (2020) 103417. <https://doi.org/10.1016/j.rinp.2020.103417>.

- [4] V.A. Khomchenko, D.A. Kiselev, J.M. Vieira, L. Jian, A.L. Kholkin, A.M.L. Lopes, Y.G. Pogorelov, J.P. Araujo, M. Maglione, Effect of diamagnetic Ca, Sr, Pb, and Ba substitution on the crystal structure and multiferroic properties of the BiFeO₃ perovskite, *J. Appl. Phys.* 103 (2008).
<https://doi.org/10.1063/1.2836802>.
- [5] E. Hern, Synthesis and magnetic characterization of LaMnO₃ nanoparticles, (2015).
- [6] Q. Lin, J. Lin, X. Yang, Y. He, L. Wang, J. Dong, The effects of Mg²⁺ and Ba²⁺ dopants on the microstructure and magnetic properties of doubly-doped LaFeO₃ perovskite catalytic nanocrystals, *Ceram. Int.* 45 (2019) 3333–3340. <https://doi.org/10.1016/j.ceramint.2018.10.246>.
- [7] H. Huang, Q. Liu, B. Lu, X. Wang, J. Hu, Diamond & Related Materials LaMnO₃-diamond composites as efficient oxygen reduction reaction catalyst for Zn-air battery, 91 (2019) 199–206.
<https://doi.org/10.1016/j.diamond.2018.11.024>.
- [8] J. Hu, L. Zhang, B. Lu, X. Wang, H. Huang, LaMnO₃ nanoparticles supported on N doped porous carbon as efficient photocatalyst, 159 (2019) 59–68. <https://doi.org/10.1016/j.vacuum.2018.10.021>.
- [9] T. Shou, Y. Li, M.T. Bernards, C. Becco, G. Cao, Y. Shi, Y. He, Degradation of gas-phase o-xylene via combined non-thermal plasma and Fe doped LaMnO₃ catalysts: Byproduct control, 387 (2020).
<https://doi.org/10.1016/j.jhazmat.2019.121750>.
- [10] F. Li, Z. Wang, A. Wang, S. Wu, L. Zhang, N-type LaFe_{1-x}Mn_xO₃ prepared by sol-gel method for gas sensing, 816 (2020) 3–7. <https://doi.org/10.1016/j.jallcom.2019.152647>.
- [11] P. Goel, S. Sundriyal, V. Shrivastav, S. Mishra, D.P. Dubal, K.-H. Kim, A. Deep, Perovskite materials as superior and powerful platforms for energy conversion and storage applications, *Nano Energy.* 80 (2021) 105552. <https://doi.org/10.1016/j.nanoen.2020.105552>.
- [12] K. Sebayang, D. Aryanto, S. Simbolon, C. Kurniawan, S.F. Hulu, T. Sudiro, M. Ginting, P. Sebayang, Effect of sintering temperature on the microstructure, electrical and magnetic properties of Zn_{0.98}Mn_{0.02}O material, *IOP Conf. Ser. Mater. Sci. Eng.* 309 (2018) 0–8. <https://doi.org/10.1088/1757-899X/309/1/012119>.
- [13] W. Azouzi, W. Sigle, H. Labrim, M. Benaissa, Sol-gel synthesis of nanoporous LaFeO₃ powders for solar applications, *Mater. Sci. Semicond. Process.* 104 (2019) 104682.
<https://doi.org/10.1016/j.mssp.2019.104682>.
- [14] K. Bhoi, T. Dam, S.R. Mohapatra, M.M. Patidar, D. Singh, A.K. Singh, P.N. Vishwakarma, P.D. Babu, V. Siruguri, D.K. Pradhan, Studies of magnetic phase transitions in orthorhombic DyMnO₃ ceramics prepared by acrylamide polymer gel template method, *J. Magn. Mater.* (2019).
<https://doi.org/10.1016/j.jmmm.2019.02.069>.

- [15] Q. Sun, X. Luo, Q. Xia, Y. Guo, J. Su, Q. Li, G. Miao, Enhanced ferromagnetism and conductivity in epitaxial LaMnO_3 thin films by oxygen-atmosphere annealing, *J. Magn. Mater.* 499 (2020). <https://doi.org/10.1016/j.jmmm.2019.166317>.
- [16] N. Geetha, S.K. V. D. Prakash, Synthesis and characterization of $\text{LaMn}_{1-x}\text{Fe}_x\text{O}_3$ ($x=0, 0.1, 0.2$) by coprecipitation route, *J. Phys. Chem. Biophys.* 8 (2018) 1–6. <https://doi.org/10.4172/2161-0398.1000273>.
- [17] L. Nejati Moghadam, Z. Rashidi Ranjbar, Cost-efficient solar cells using nanocrystalline perovskite $\text{La}(\text{Fe and Mn})\text{O}_3$ and candle soot: Theory and experiment, *J. Alloys Compd.* 785 (2019) 117–124. <https://doi.org/10.1016/j.jallcom.2019.01.068>.
- [18] A. Moghtada, R. Ashiri, Enhancing the formation of tetragonal phase in perovskite nanocrystals using an ultrasound assisted wet chemical method, *Ultrason. - Sonochemistry.* 33 (2016) 141–149. <https://doi.org/10.1016/j.ultsonch.2016.05.002>.
- [19] G. Deng, Y. Chen, M. Tao, C. Wu, X. Shen, H. Yang, M. Liu, Electrochimica Acta Electrochemical properties and hydrogen storage mechanism of perovskite-type oxide LaFeO_3 as a negative electrode for Ni / MH batteries, 55 (2010) 1120–1124. <https://doi.org/10.1016/j.electacta.2009.09.078>.
- [20] A. Giroir-fendler, M. Alves-fortunato, M. Richard, C. Wang, J. Antonio, S. Gil, C. Zhang, F. Can, N. Bion, Applied Catalysis B: Environmental Synthesis of oxide supported LaMnO_3 perovskites to enhance yields in toluene combustion, "Applied Catal. B, Environ. 180 (2016) 29–37. <https://doi.org/10.1016/j.apcatb.2015.06.005>.
- [21] A. Daundkar, S.N. Kale, S.P. Gokhale, V. Ravi, A low temperature route to prepare LaMnO_3 , 60 (2006) 1213–1214. <https://doi.org/10.1016/j.matlet.2005.11.002>.
- [22] C. Zhang, Y. Guo, Y. Guo, G. Lu, A. Boreave, L. Retailleau, A. Baylet, A. Giroir-fendler, Applied Catalysis B: Environmental LaMnO_3 perovskite oxides prepared by different methods for catalytic oxidation of toluene, "Applied Catal. B, Environ. 148–149 (2014) 490–498. <https://doi.org/10.1016/j.apcatb.2013.11.030>.
- [23] O.P. Taran, A.B. Ayusheev, O.L. Ogorodnikova, I.P. Prosvirin, L.A. Isupova, V.N. Parmon, Applied Catalysis B: Environmental Perovskite-like catalysts LaBO_3 ($B = \text{Cu}, \text{Fe}, \text{Mn}, \text{Co}, \text{Ni}$) for wet peroxide oxidation of phenol, "Applied Catal. B, Environ. 180 (2016) 86–93. <https://doi.org/10.1016/j.apcatb.2015.05.055>.
- [24] M. Shaterian, M. Enhessari, D. Rabbani, M. Asghari, Synthesis, characterization and photocatalytic activity of LaMnO_3 nanoparticles, *Appl. Surf. Sci.* 318 (2014) 213–217. <https://doi.org/10.1016/j.apsusc.2014.03.087>.

- [25] F. Lamno, T. Phan, P.Q. Thanh, P.D.H. Yen, P. Zhang, T.D. Thanh, S.C. Yu, Ferromagnetic short-range order and magnetocaloric effect, 167 (2013) 49–53. <https://doi.org/10.1016/j.ssc.2013.06.009>.
- [26] W. Haron, A. Wisitsoraat, S. Wongnawa, Nanostructured perovskite oxides – LaMO₃ (M=Al, Co, Fe) prepared by co-precipitation method and their ethanol-sensing characteristics, *Ceram. Int.* (2017). <https://doi.org/10.1016/j.ceramint.2017.01.013>.
- [27] J.L. Ortiz-Quiñonez, L. García-González, F.E. Cancino-Gordillo, U. Pal, Particle dispersion and lattice distortion induced magnetic behavior of La_{1-x}Sr_xMnO₃ perovskite nanoparticles grown by salt-assisted solid-state synthesis, *Mater. Chem. Phys.* 246 (2020). <https://doi.org/10.1016/j.matchemphys.2020.122834>.
- [28] A. Ashok, A. Kumar, J. Ponraj, S.A. Mansour, F. Tarlochan, Enhancing the electrocatalytic properties of LaMnO₃ by tuning surface oxygen deficiency through salt assisted combustion synthesis, *Catal. Today.* (2020) 0–1. <https://doi.org/10.1016/j.cattod.2020.05.065>.
- [29] S.Y. Lee, J. Yun, W.P. Tai, Synthesis of Ni-doped LaSrMnO₃ nanopowders by hydrothermal method for SOFC interconnect applications, *Adv. Powder Technol.* 29 (2018) 2423–2428. <https://doi.org/10.1016/j.appt.2018.06.021>.
- [30] N. Das, D. Bhattacharya, A. Sen, H.S. Maiti, Sonochemical synthesis of LaMnO₃ nano-powder, *Ceram. Int.* 35 (2009) 21–24. <https://doi.org/10.1016/j.ceramint.2007.09.002>.
- [31] R. Pelosato, C. Cristiani, G. Dotelli, M. Mariani, A. Donazzi, I. Natali Sora, Co-precipitation synthesis of SOFC electrode materials, *Int. J. Hydrogen Energy.* 38 (2013) 480–491. <https://doi.org/10.1016/j.ijhydene.2012.09.063>.
- [32] G. Qin, X. Huang, J. Chen, Z. He, Synthesis of Sr and Mg double-doped LaAlO₃ nanopowders via EDTA-glycine combined process, *Powder Technol.* 235 (2013) 880–885. <https://doi.org/10.1016/j.powtec.2012.11.048>.
- [33] K. Navin, R. Kurchania, Structural, magnetic and electrochemical properties of LSMO-ZnO core-shell nanostructure, *Mater. Chem. Phys.* 234 (2019) 25–31. <https://doi.org/10.1016/j.matchemphys.2019.05.083>.
- [34] C. Li, J. Cheng, Y. Jiang, W. Xiao, X. Yan, Synthesis and enhanced electrocatalytic mechanism of mesoporous La_{0.8}Sr_{0.2}MnO₃ nanowires as high-active electrocatalysts for Zn-air batteries, *Appl. Surf. Sci.* 538 (2021) 148015. <https://doi.org/10.1016/j.apsusc.2020.148015>.
- [35] H. Luo, J. Guo, T. Shen, H. Zhou, J. Liang, S. Yuan, Study on the catalytic performance of LaMnO₃ for the RhB degradation, *J. Taiwan Inst. Chem. Eng.* 109 (2020) 15–25. <https://doi.org/10.1016/j.jtice.2020.01.011>.

- [36] Y. Song, Z. Wang, Y. Yan, M. Zhang, G. Wang, T. Yin, Y. Xue, F. Gao, M. Qiu, Molten salt synthesis and supercapacitor properties of oxygen-vacancy, 43 (2020) 173–181.
<https://doi.org/10.1016/j.jechem.2019.09.007>.
- [37] S. Priyatharshni, S.R. Kumar, C. Viswanathan, N. Ponpandian, Morphologically tuned LaMnO₃ as an efficient nanocatalyst for the removal of organic dye from aqueous solution under sunlight, J. Environ. Chem. Eng. 8 (2020) 104146. <https://doi.org/10.1016/j.jece.2020.104146>.
- [38] D. Çoban Özkan, A. Türk, E. Çelik, Synthesis and characterizations of sol–gel derived LaFeO₃ perovskite powders, J. Mater. Sci. Mater. Electron. 31 (2020) 22789–22809.
<https://doi.org/10.1007/s10854-020-04803-8>.
- [39] . E. Celik, U. Aybarc, M.F. Ebeoglugil, I. Birlik, O. Culha, ITO films on glass substrate by sol – gel technique: synthesis , characterization and optical properties, J. Sol–Gel. Sci. Technol. 50 (2009) 337–347. <https://doi.org/10.1007/s10971-009-1931-4>.
- [40] P. Hu, H. Yang, D. Pan, H. Wang, J. Tian, S. Zhang, X. Wang, A.A. Volinsky, Heat treatment effects on microstructure and magnetic properties of Mn – Zn ferrite powders, J. Magn. Mater. 322 (2010) 173–177. <https://doi.org/10.1016/j.jmmm.2009.09.002>.
- [41] A. Dimian, C. Bildea, A. Kiss, Integrated Design and Simulation of Chemical Processes, 2014.
<https://doi.org/10.1016/B978-0-444-62700-1.09993-9>.
- [42] Chaudhery Mustansar Hussain, ed., Handbook of Nanomaterials for Industrial Applications, 2018.
<https://doi.org/10.1016/C2016-0-04427-3>.
- [43] T. Jia, Z. Zeng, H.Q. Lin, Y. Duan, P. Ohodnicki, First-principles study on the electronic, optical and thermodynamic properties of ABO₃ (A = La,Sr, B = Fe,Co) perovskites, RSC Adv. (2017) 38798–38804.
<https://doi.org/10.1039/c7ra06542f>.
- [44] R. Rauer, Optical Spectroscopy of Strongly Correlated Transition-metal Oxides, Cuvillier Verlag, 2005.
- [45] K.M.S. Khalil, W.A. Elhamdy, A.E.A. Said, A.A. Elsamahy, Porous LaFeO₃ / Silica Nanocomposites via Sol-Gel Mixing Involving Citric Acid, Colloids Surfaces A Physicochem. Eng. Asp. 506 (2016) 840–848.
<https://doi.org/10.1016/j.colsurfa.2016.07.068>.
- [46] E. Cao, Y. Yang, T. Cui, Y. Zhang, W. Hao, L. Sun, H. Peng, X. Deng, Effect of synthesis route on electrical and ethanol sensing characteristics for LaFeO_{3-δ} nanoparticles by citric sol-gel method, Appl. Surf. Sci. 393 (2017) 134–143. <https://doi.org/10.1016/j.apsusc.2016.10.013>.
- [47] J.D. Wright, Sol-Gel Materials, CRC Press, 2018.
- [48] J. Wang, X. Cao, S. Liu, Y. Guo, Z. Wang, X. Li, Y. Ren, Z. Xia, H. Wang, C. Liu, N. Wang, W. Jiang, W. properties of AZO nanoparticles by sol- gel combustion

method, *Ceram. Int.* (2020) 0–1. <https://doi.org/10.1016/j.ceramint.2020.04.068>.

[49] L. Sr, M. Fe, Sol – gel synthesis , characterization and microwave absorbing properties, *Mater. Res. Bull.* 47 (2012) 1961–1967. <https://doi.org/10.1016/j.materresbull.2012.04.017>.

[50] A.C. Pierre, *Introduction to sol-gel processing*, Springer US, Boston, 1998. <https://doi.org/10.1007/978-1-4615-5659-6>.

[51] C.J. Brinker, G.W. Scherer, *Sol-gel science: the physics and chemistry of sol-gel processing*, San Diego, 1990.

[52] K. Vojisavljević, P. Chevreux, J. Jouin, B. Malič, Characterization of the alkoxide-based sol-gel derived $\text{La}_9\text{Si}_6\text{O}_{26}$ powder and ceramic, *Acta Chim. Slov.* 61 (2014) 530–541.

[53] M. Yurddaskal, E. Celik, Effect of halogen-free nanoparticles on the mechanical, structural, thermal and flame retardant properties of polymer matrix composite, *Compos. Struct.* 183 (2017) 381–388. <https://doi.org/10.1016/j.compstruct.2017.03.093>.

[54] P. V Gosavi, R.B. Biniwale, Pure phase LaFeO_3 perovskite with improved surface area synthesized using different routes and its characterization, 119 (2010) 324–329. <https://doi.org/10.1016/j.matchemphys.2009.09.005>.

[55] X. Chen, J. Yu, S. Guo, S. Lu, Z. Luo, M. He, Surface modification of magnesium hydroxide and its application in flame retardant polypropylene composites, *J. Mater. Sci.* 44 (2009) 1324–1332. <https://doi.org/10.1007/s10853-009-3273-6>.

[56] E. SPAHIU, ATR-FTIR EVALUATION OF STRUCTURAL AND FUNCTIONAL CHANGES ON MURINE MACROPHAGE CELLS UPON ACTIVATION AND SUPPRESSION BY IMMUNO-THERAPEUTIC OLIGODEOXYNUCLEOTIDES, MIDDLE EAST TECHNICAL UNIVERSITY, 2015.

[57] L. Lin, Z. Song, Z. Haider, X. Liu, W. Qiu, Enhanced As (III) removal from aqueous solution by Fe-Mn-La- impregnated biochar composites, *Sci. Total Environ.* 686 (2019) 1185–1193. <https://doi.org/10.1016/j.scitotenv.2019.05.480>.

[58] M. Sukumar, L.J. Kennedy, J.J. Vijaya, B. Al-Najar, M. Bououdina, Facile synthesis of Fe^{3+} doped $\text{La}_2\text{CuO}_4/\text{LaFeO}_3$ perovskite nanocomposites: Structural, optical, magnetic and catalytic properties, *Mater. Sci. Semicond. Process.* 100 (2019) 225–235. <https://doi.org/10.1016/j.mssp.2019.04.049>.

[59] and M.R.M. A. Monshi, M. R. Foroughi, Modified Scherrer equation to estimate more accurately nano-crystallite size using XRD, *World J. Nano Sci. Eng.* 2 (2012) 154–160.

[60] H. Gao, C. Zheng, H. Yang, X. Niu, S. Wang, Construction of a CQDs / Ag_3PO_4 / BiPO_4 Heterostructure Photocatalyst with Enhanced Photocatalytic Degradation of Rhodamine B under

- [61] S. Guan, H. Yang, X. Sun, T. Xian, Preparation and promising application of novel LaFeO₃/BiOBr heterojunction photocatalysts for photocatalytic and photo-Fenton removal of dyes, *Opt. Mater. (Amst)*. 100 (2020) 109644. <https://doi.org/10.1016/j.optmat.2019.109644>.
- [62] R.G.H. A. J. Signorelli, X-Ray Photoelectron Spectroscopy of Various Core Levels of Lanthanide Ions: The Roles of Monopole Excitation and Electrostatic Coupling, *Phys. Rev. B (Covering Condens. Matter Mater. Physics)*. 8 (1973).
- [63] E.B. Simsek, Ö. Tuna, Z. Balta, Separation and Purification Technology Construction of stable perovskite-type LaFeO₃ particles on polymeric resin with boosted photocatalytic Fenton-like decaffeination under solar irradiation, *Sep. Purif. Technol.* 237 (2020) 116384. <https://doi.org/10.1016/j.seppur.2019.116384>.
- [64] F.J. Maldonado-Hódar, H. Jirglová, S. Morales-Torres, A.F. Pérez-Cadenas, Influence of surfactants on the physicochemical properties and catalytic behaviour of Mo-doped carbon xerogels, *Catal. Today*. 301 (2018) 217–225. <https://doi.org/10.1016/j.cattod.2017.01.030>.
- [65] A.-M. HERMANS SON, Microstructure of protein gels related to functionality, in: R.Y. YADA, R.L. JACKMAN, J.L. SMITH (Eds.), *Protein Struct. Relationships Foods*, SPRINGER SCIENCE+BUSINESS MEDIA, LLC, 1994: p. 202.
- [66] I. Jaouali, H. Hamrouni, N. Moussa, M.F. Nsib, M. Angel, A. Bonavita, G. Neri, S. Gianluca, LaFeO₃ ceramics as selective oxygen sensors at mild temperature, *Ceram. Int.* 44 (2018) 4183–4189. <https://doi.org/10.1016/j.ceramint.2017.11.221>.
- [67] Zetasizer Nano User Manual, Malvern Instruments Ltd., 2013., (n.d.).
- [68] Y.T. O, J.B. Koo, K.J. Hong, J.S. Park, D.C. Shin, Effect of grain size on transmittance and mechanical strength of sintered alumina, *Mater. Sci. Eng. A*. 374 (2004) 191–195. <https://doi.org/10.1016/j.msea.2004.02.015>.
- [69] J. Piprek, *Semiconductor Optoelectronic Devices: Introduction to Physics and Simulation*, 2013. <https://doi.org/10.1016/B978-0-08-046978-2.50029-6>.
- [70] V. Gruzdev, Ultrafast laser-induced modifications of energy bands of non-metal crystals, *Proc. SPIE*. 7501 (2009). <https://doi.org/10.1117/12.836908>.
- [71] S.P. Ghorpade, R.H. Krishna, R.M. Melavanki, V. Dubey, Effect of Eu³⁺ on optical and energy bandgap of SrY₂O₄ nanophosphors for FED applications, *Opt. - Int. J. Light Electron Opt.* 208 (2020) 164533. <https://doi.org/10.1016/j.ijleo.2020.164533>.
- [72] R. Köferstein, L. Jäger, S.G. Ebbinghaus, Magnetic and optical investigations on LaFeO₃ powders with different particle sizes and corresponding ceramics, *Solid State Ionics*. 249–250 (2013) 1–5.

- [73] D. Ramírez-ortega, I. González, R. Arroyo, Semiconducting properties of ZnO / TiO₂ composites by electrochemical measurements and their relationship with photocatalytic activity *Electrochimica Acta Semiconducting properties of ZnO / TiO₂ composites by electrochemical measurements and their relationship with photocatalytic activity*, (2014) 2–11. <https://doi.org/10.1016/j.electacta.2014.06.060>.
- [74] D. Ramírez-ortega, D. Guerrero-araque, D. Ramírez-ortega, P. Acevedo-peña, Interfacial Charge-Transfer Process across ZrO₂-TiO₂ Heterojunction and its Impact on Photocatalytic Activity *Journal of Photochemistry and Photobiology A: Chemistry Interfacial charge-transfer process across ZrO₂ -TiO₂ heterojunction and its impact on,* "Journal Photochem. Photobiol. A Chem. 335 (2016) 276–286. <https://doi.org/10.1016/j.jphotochem.2016.11.030>.
- [75] T. Vijayaraghavan, M. Bradha, P. Babu, K.M. Parida, G. Ramadoss, S. Vadivel, R. Selvakumar, A. Ashok, Influence of secondary oxide phases in enhancing the photocatalytic properties of alkaline earth elements doped LaFeO₃ nanocomposites, *J. Phys. Chem. Solids.* 140 (2020) 109377. <https://doi.org/10.1016/j.jpics.2020.109377>.
- [76] S.R. Kumar, C. V Abinaya, S. Amirthapandian, N. Ponpandian, Enhanced visible light photocatalytic activity of porous LaMnO₃ sub-micron particles in the degradation of rose bengal, *Mater. Res. Bull.* 93 (2017) 270–281. <https://doi.org/10.1016/j.materresbull.2017.05.024>.
- [77] M. Purnachander, S. Musthafa, J.J. Wu, S. Anandan, Facile synthesis of perovskite LaFeO₃ ferroelectric nanostructures for heavy metal ion removal applications, *Mater. Chem. Phys.* 232 (2019) 200–204. <https://doi.org/10.1016/j.matchemphys.2019.04.086>.
- [78] A. Manikandan, R. Sridhar, S.A. Antony, S. Ramakrishna, A simple aloe vera plant-extracted microwave and conventional combustion synthesis: Morphological , optical , magnetic and catalytic properties of CoFe₂O₄ nanostructures, *J. Mol. Struct.* 1076 (2014) 188–200. <https://doi.org/10.1016/j.molstruc.2014.07.054>.
- [79] Y. Slimani, M.A. Almessiere, A.D. Korkmaz, S. Guner, H. Güngüne, M. Sertkol, A. Manikandan, A. Yildiz, S. Akhtar, S.E. Shirsath, A. Baykal, Ni_{0.4}Cu_{0.2}Zn_{0.4}TbxFe_{2-x}O₄ nanospinel ferrites: Ultrasonic synthesis and physical properties, *Ultrason. - Sonochemistry.* 59 (2019). <https://doi.org/10.1016/j.ultsonch.2019.104757>.
- [80] A.M.M. Durka, S.A. Antony, A Novel Synthesis , Structural , Morphological , and Opto-magnetic Characterizations of Magnetically Separable Spinel Co_xMn_{1-x}Fe₂O₄ (0 ≤ x ≤ 1) Nano-catalysts, (2014) 2841–2857. <https://doi.org/10.1007/s10948-014-2771-1>.
- [81] A.V.T. S.V. Trukhanov , D.P. Kozlenko, High hydrostatic pressure effect on magnetic state of anion-deficient La_{0.70}Sr_{0.30}MnO_x perovskite manganites, *J. Magn. Magn. Mater.* 320 (2008) 91–94. <https://doi.org/10.1016/j.jmmm.2008.02.021>.

Figures

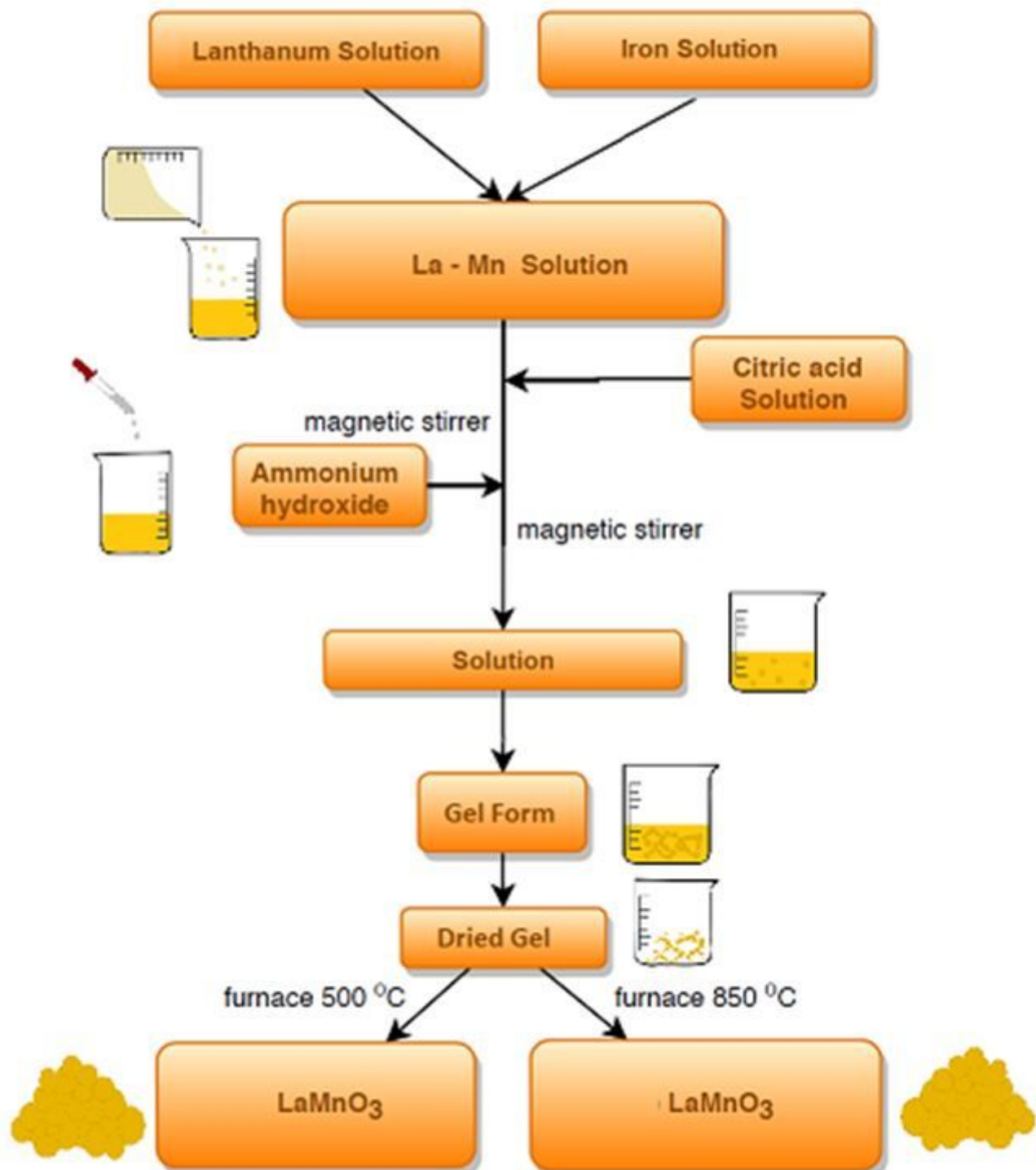


Figure 1

Flow chart of the solution and gel preparations for LaMnO₃ powder

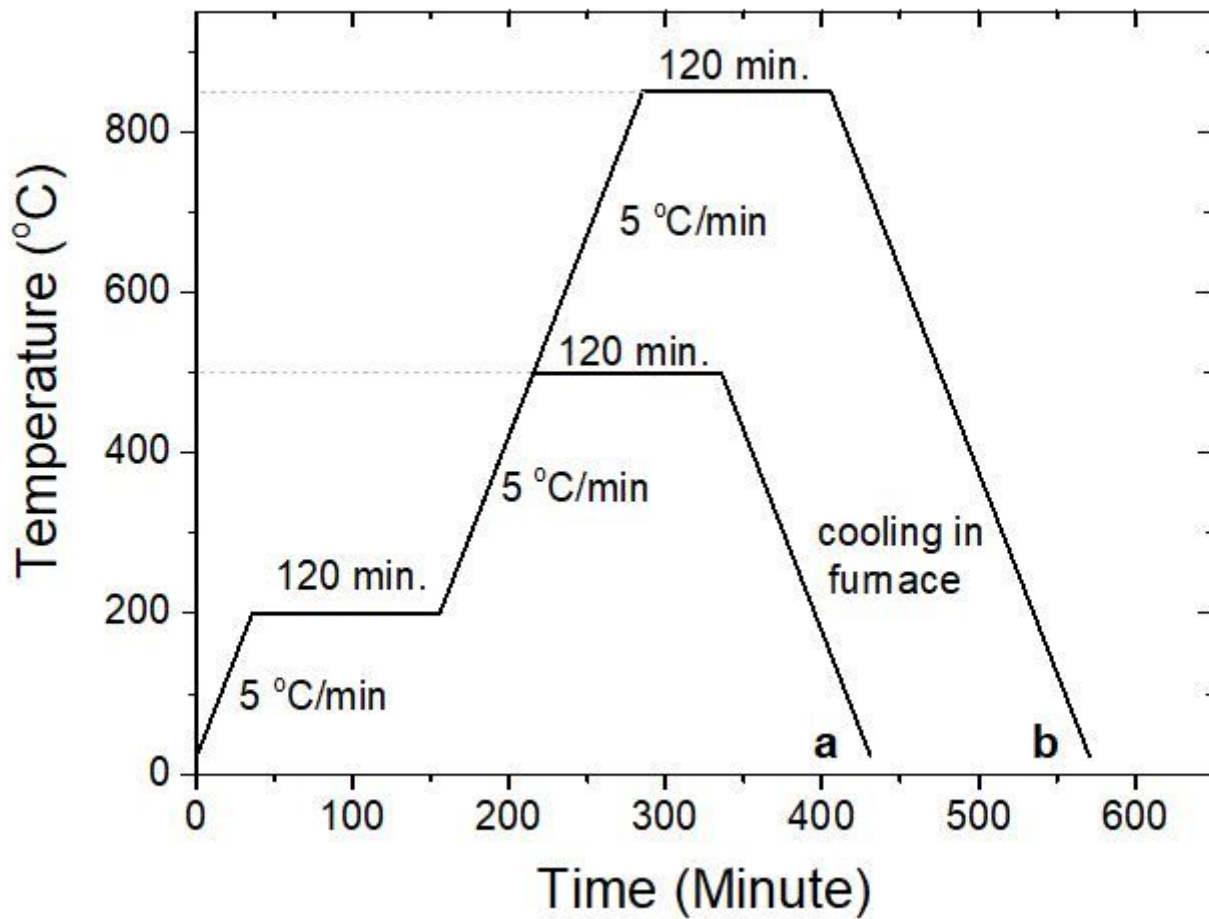


Figure 2

Heat treatment regimes for LaMnO₃ powders for (a) 500°C and (b) 850°C.

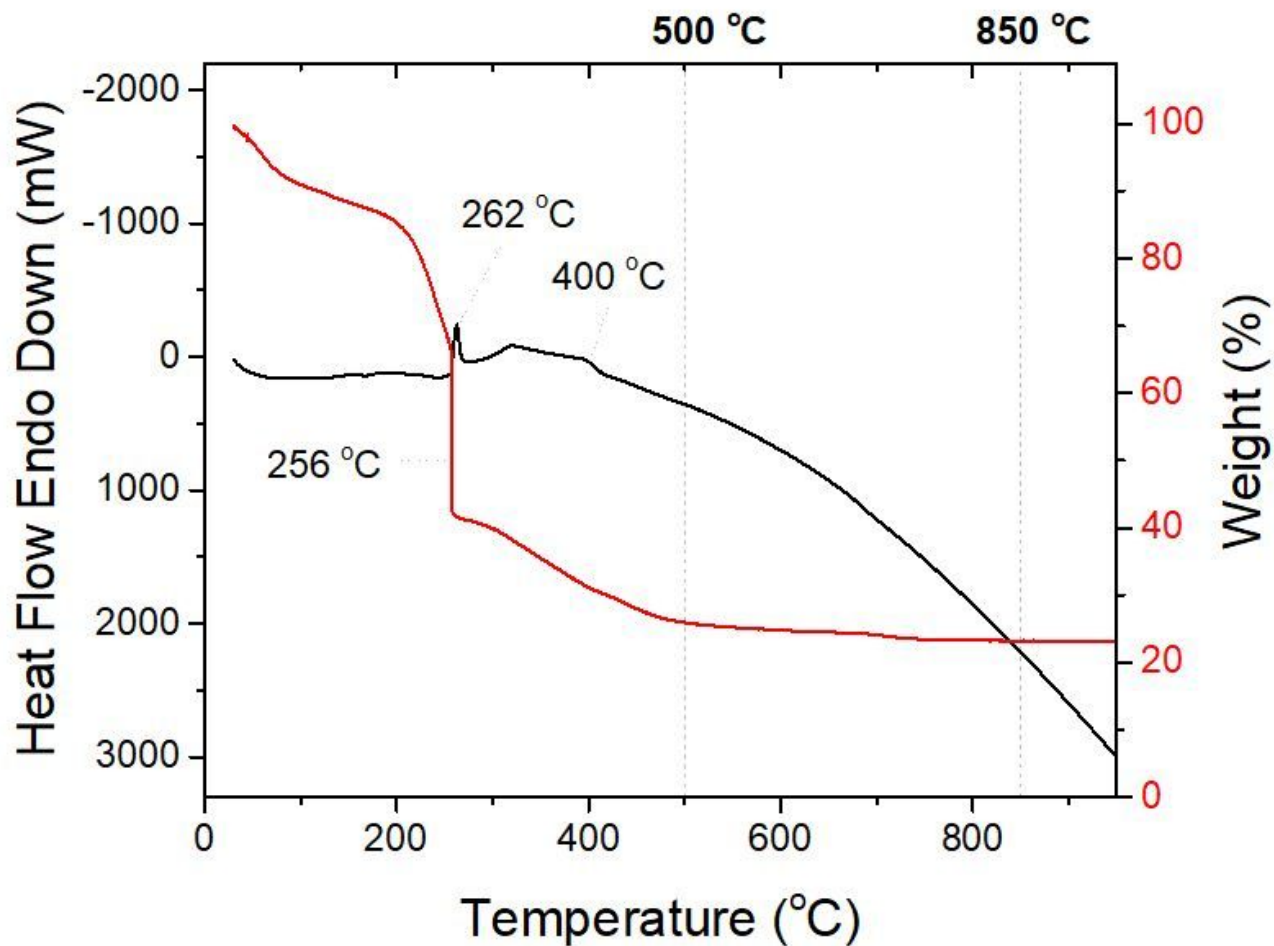


Figure 3

DTA and TGA curves of La-Mn based xerogels dried at 90 oC .

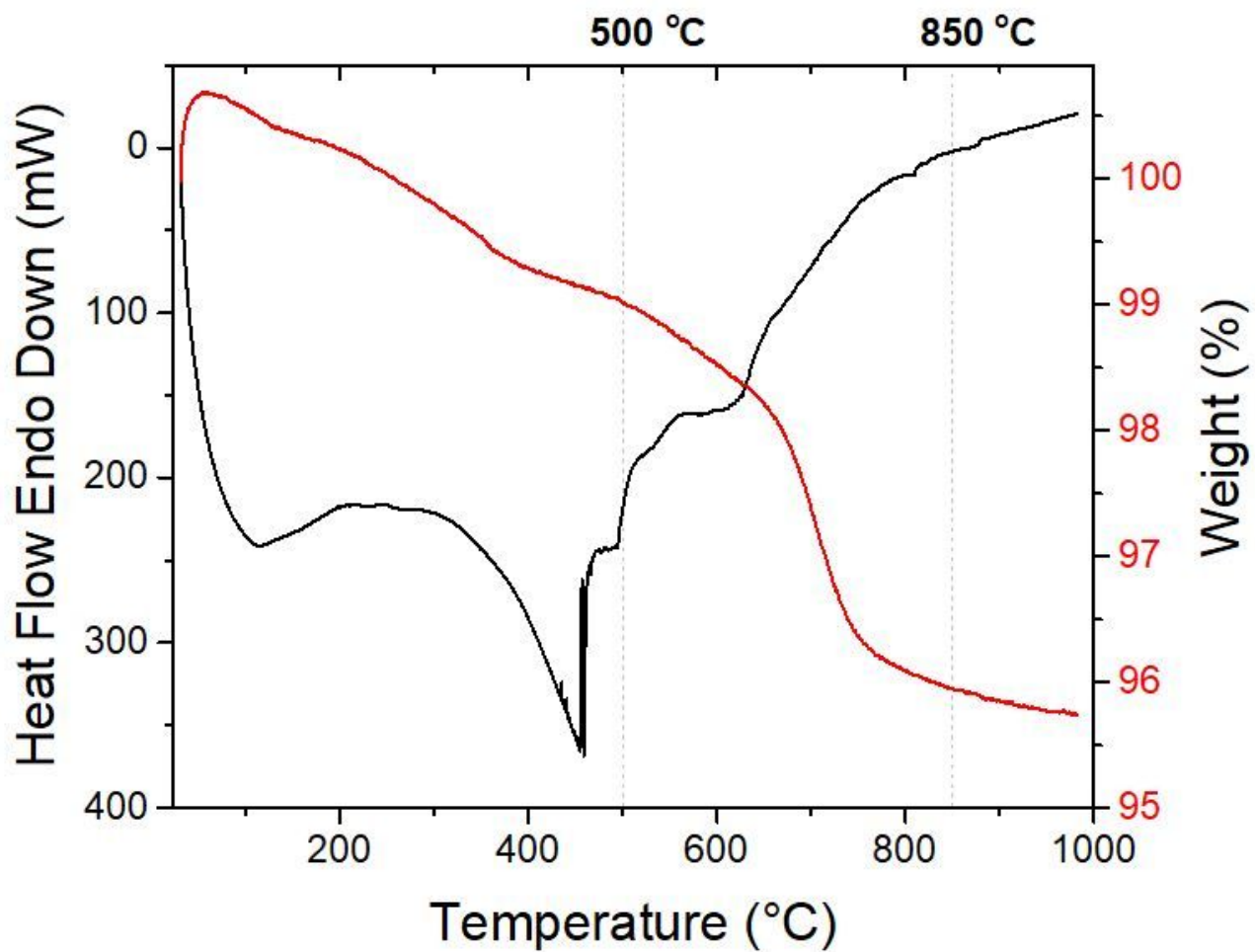


Figure 4

DTA and TGA curves of LaMnO₃ powder annealed at 500 °C .

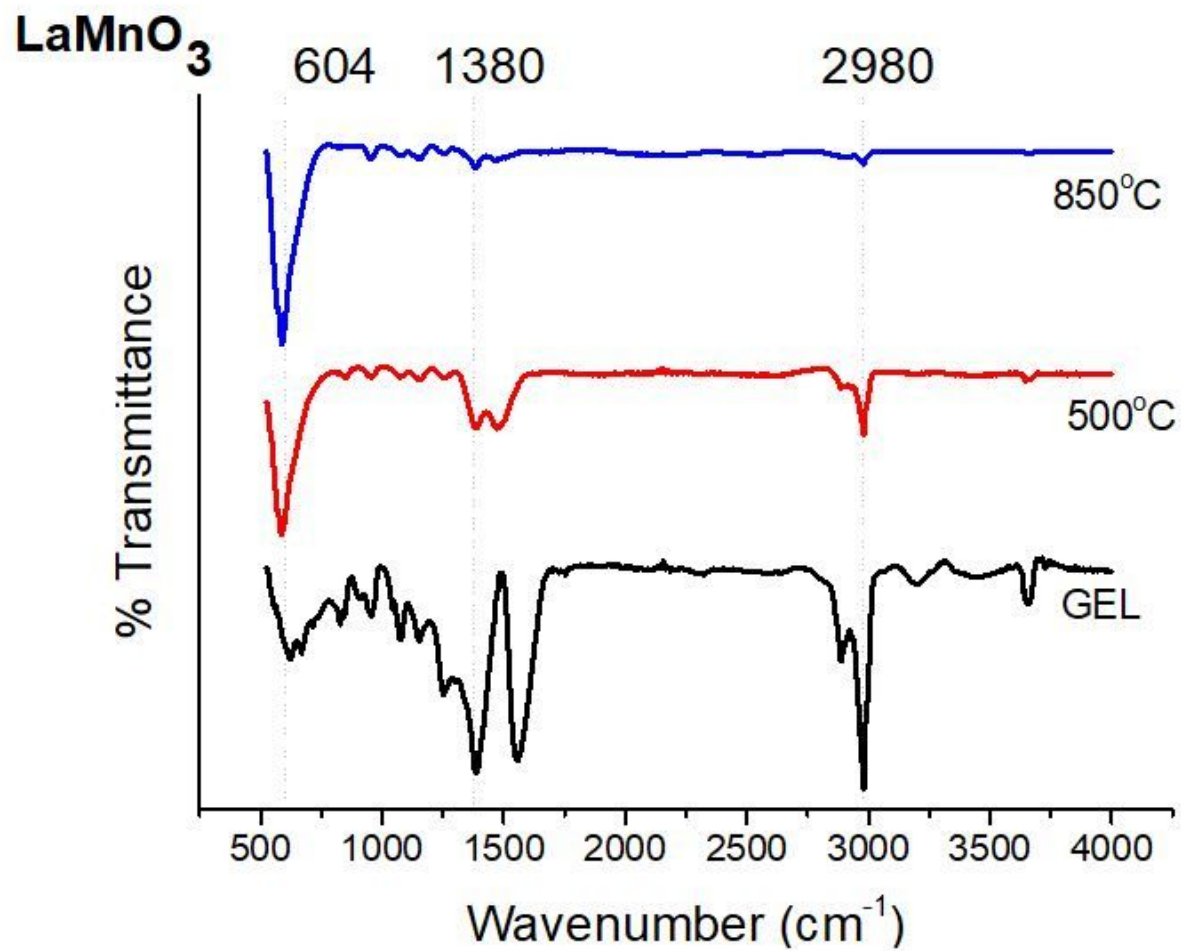


Figure 5

FTIR spectra of LaMnO_3 powders at heat treated at 90°C, 500°C and 850°C.

50-0298

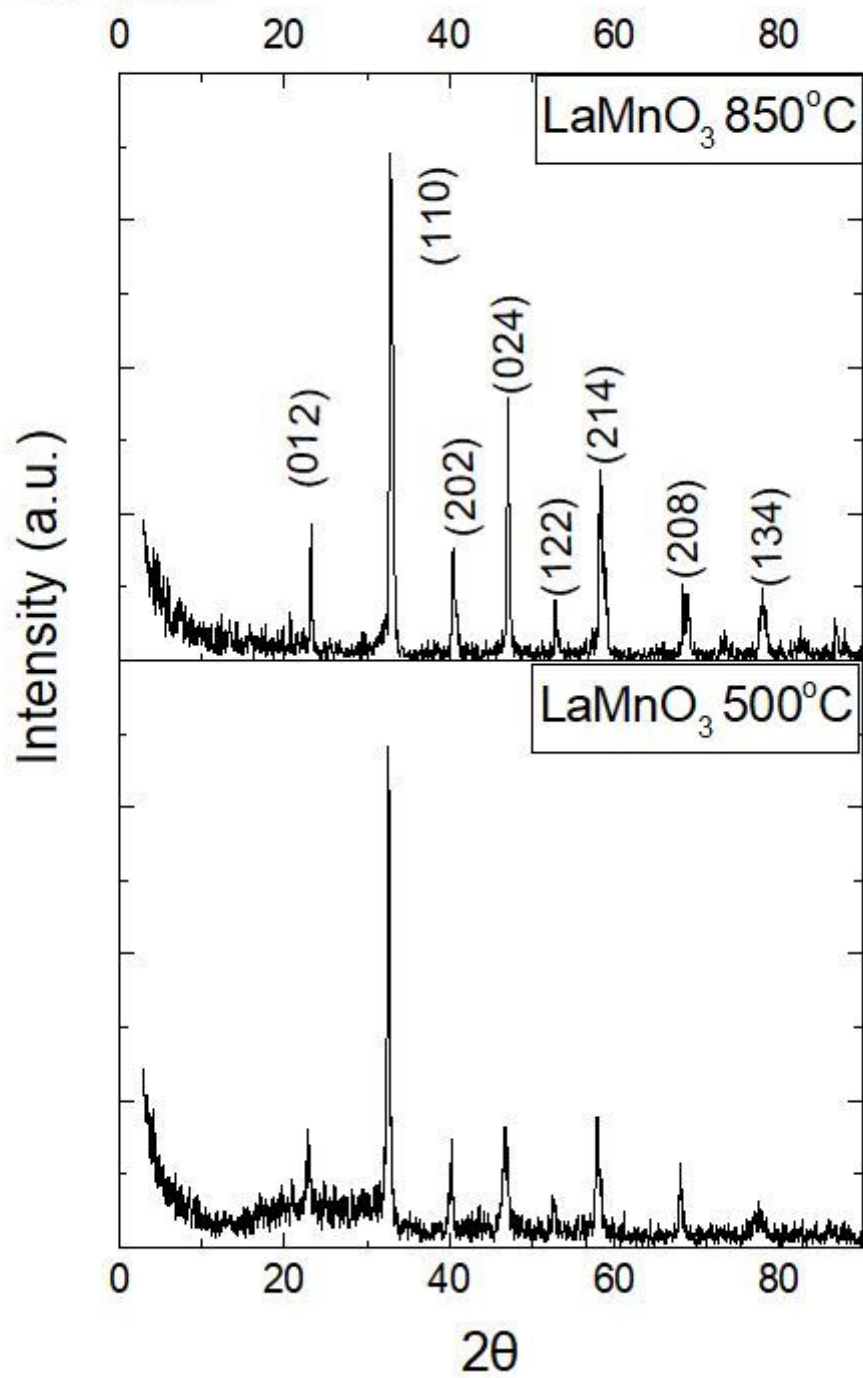
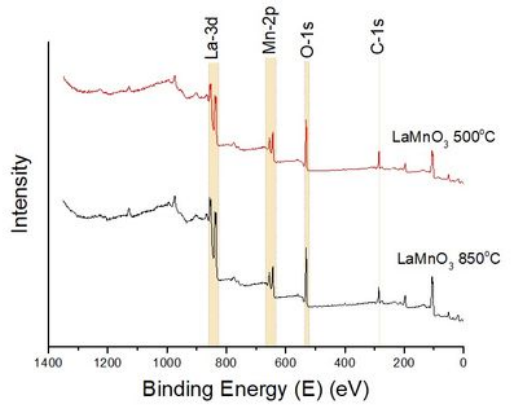
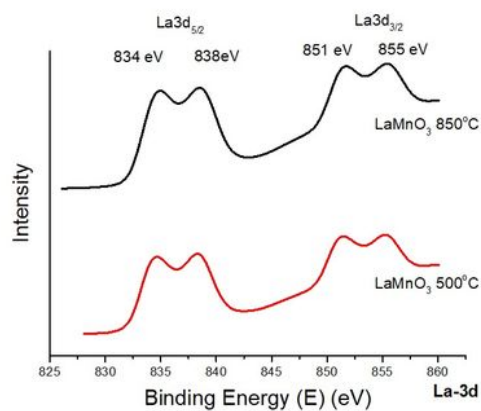


Figure 6

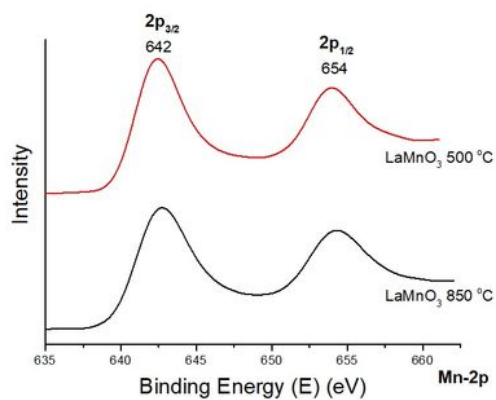
XRD patterns of LaMnO₃ powders at annealed at 500°C and 850°C.



(a)



(b)



(c)

Figure 7

(a) Survey scan XPS spectra for LaMnO₃ powders, high-resolution XPS spectra of (b) La-3d_{5/2} and (c) Mn-2p for LaMnO₃ powders

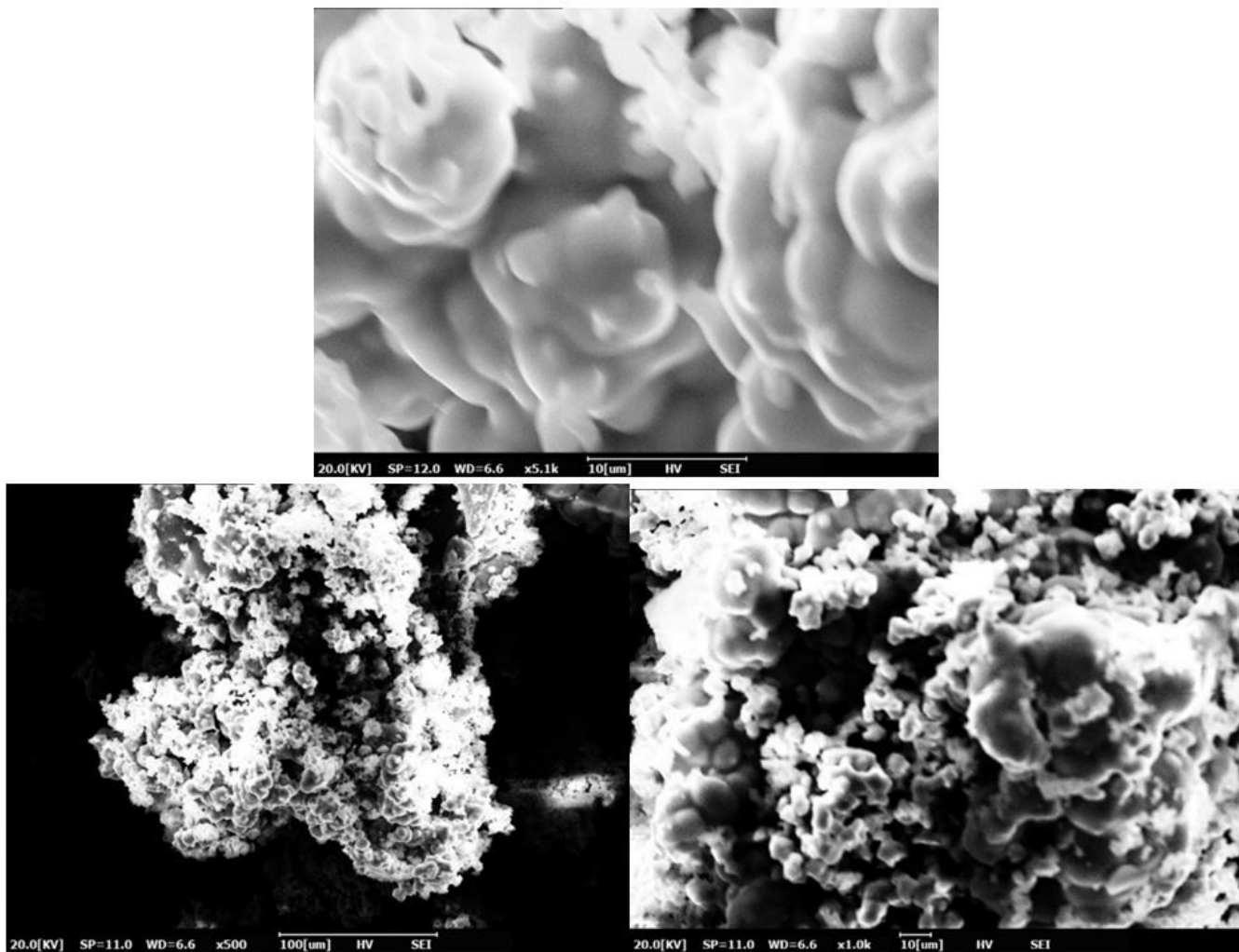
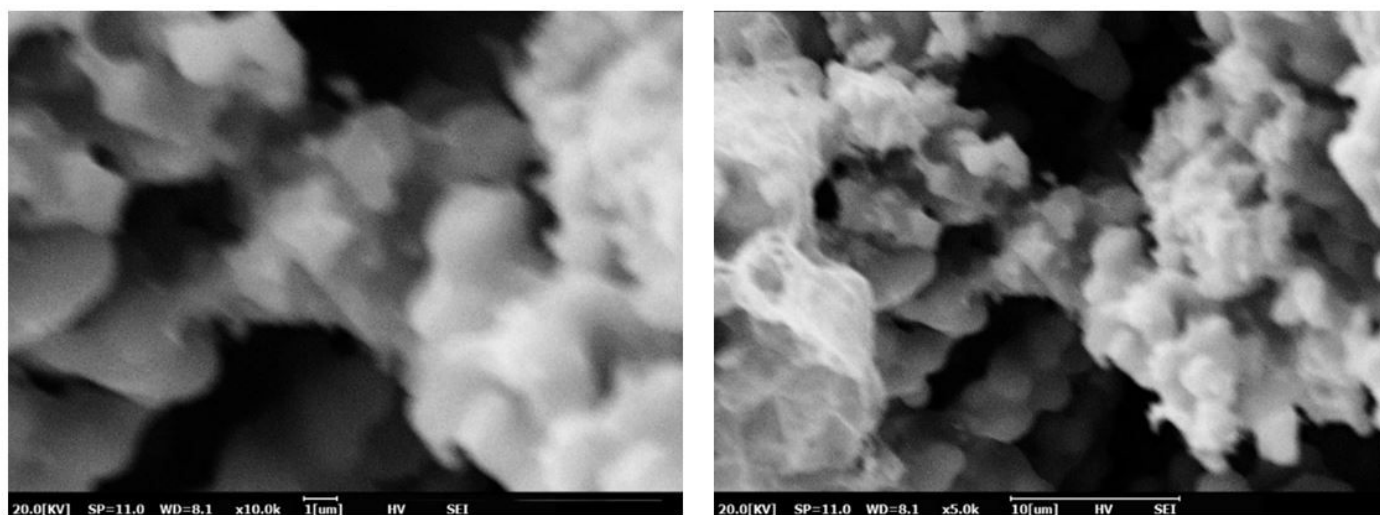


Figure 8

Surface morphologies of La-Mn based xerogel



Surface morphologies of LaMnO₃ powder annealed at 500°C

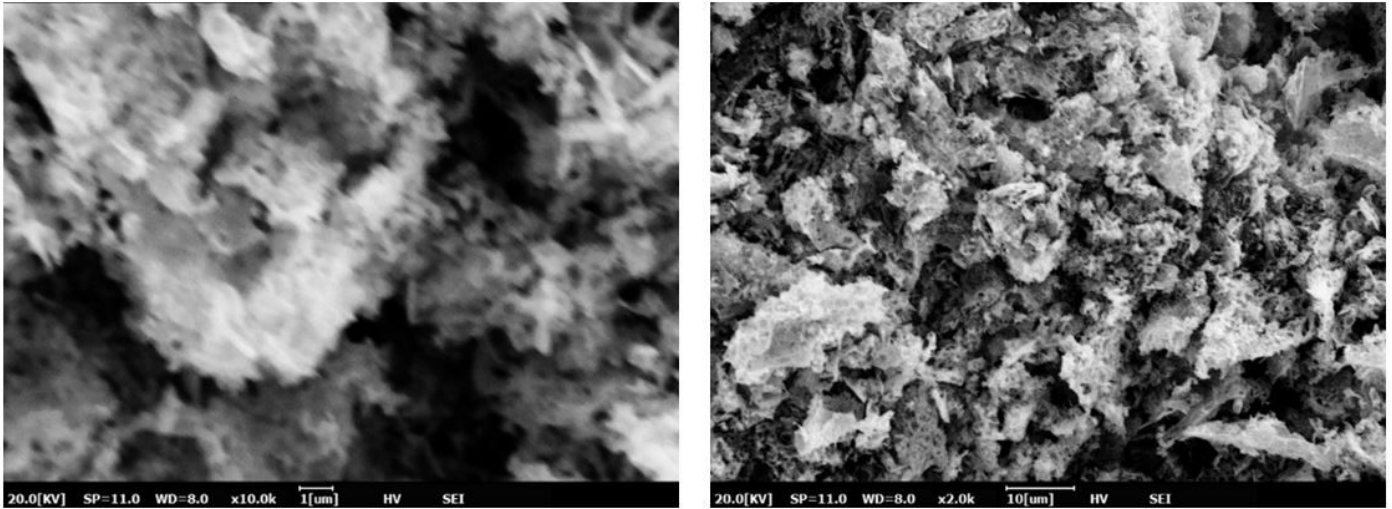
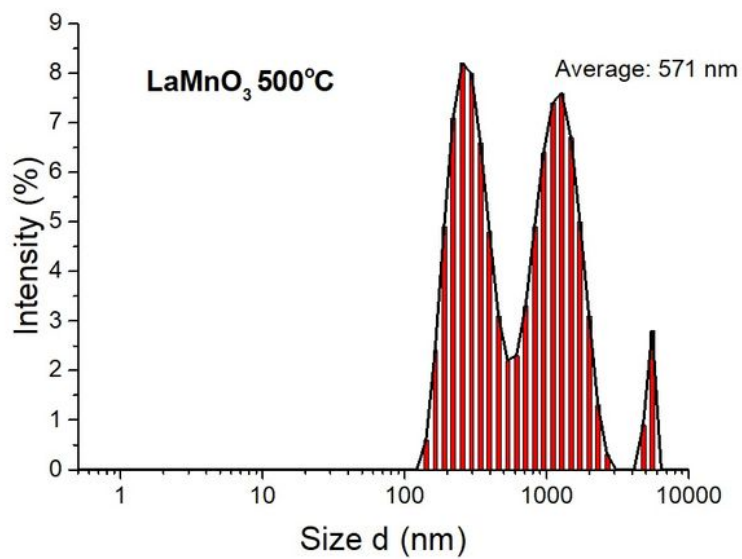
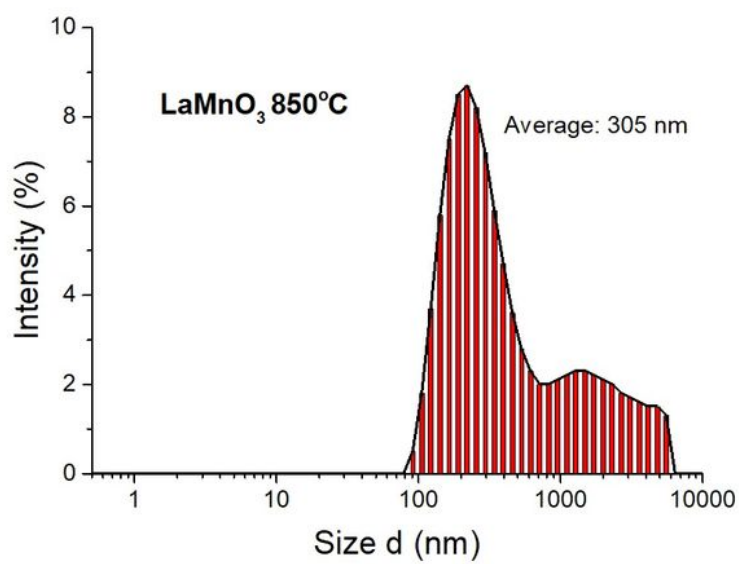


Figure 10

Surface morphologies of LaMnO₃ powder annealed at 850°C



(a)



(b)

Figure 11

Particle size distributions of LaMnO₃ powders annealed at (a) 500°C and (b) 850°C

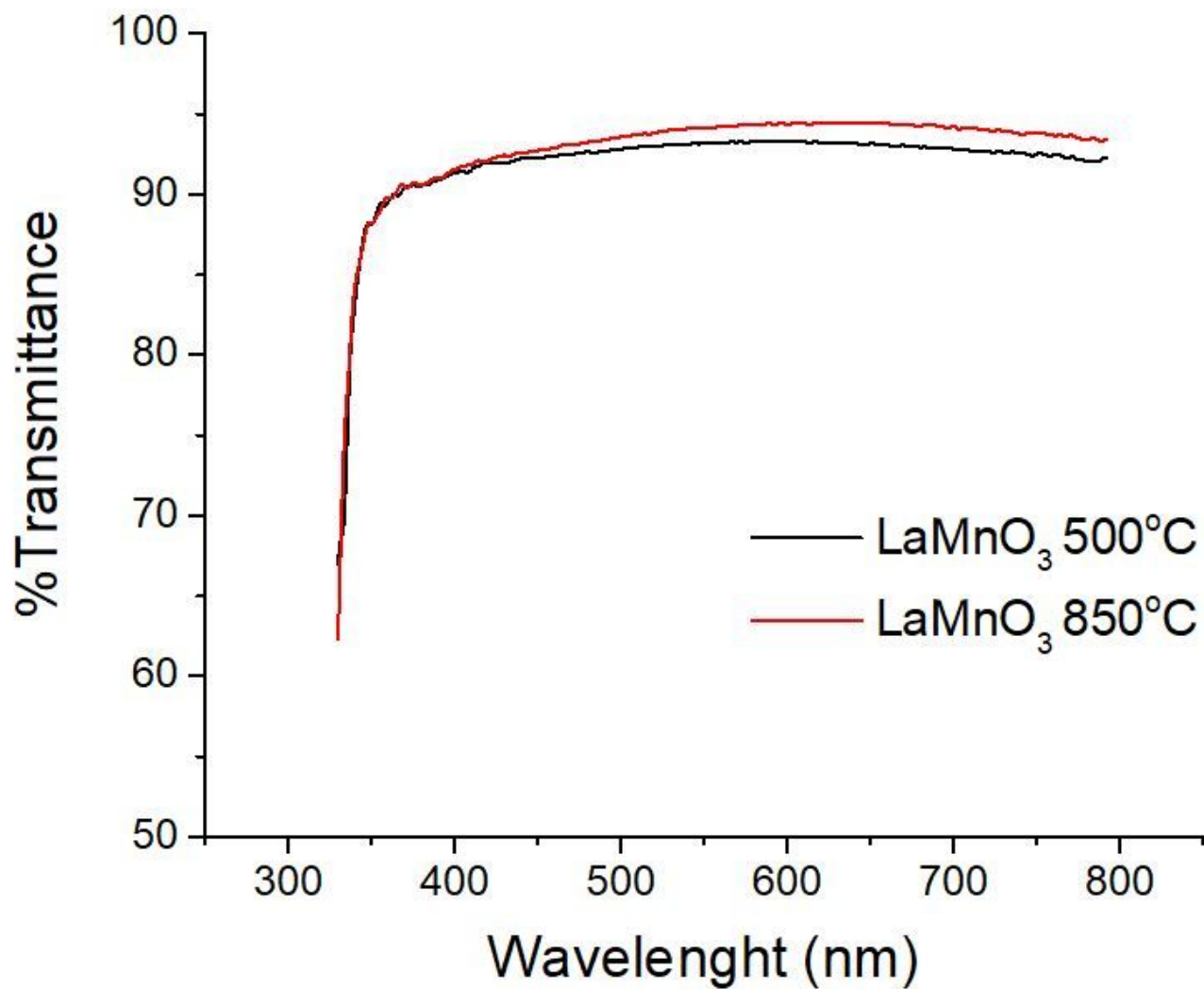


Figure 12

Transmittance Wavelength curve of LaMnO₃ powders annealed at 500°C and 850°C

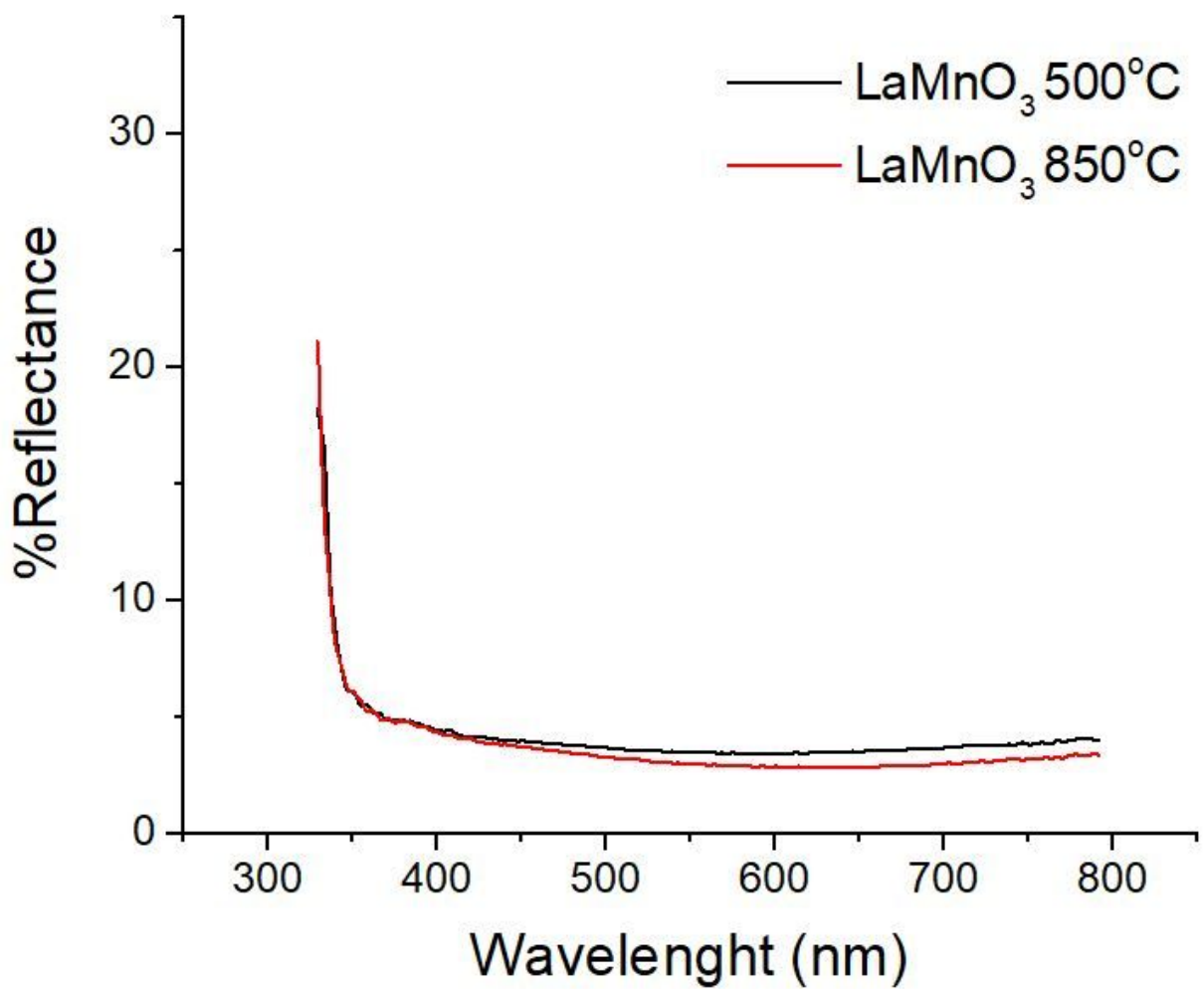


Figure 13

Reflectance - Wavelength curve of LaMnO₃ powders annealed at 500°C and 850°C .

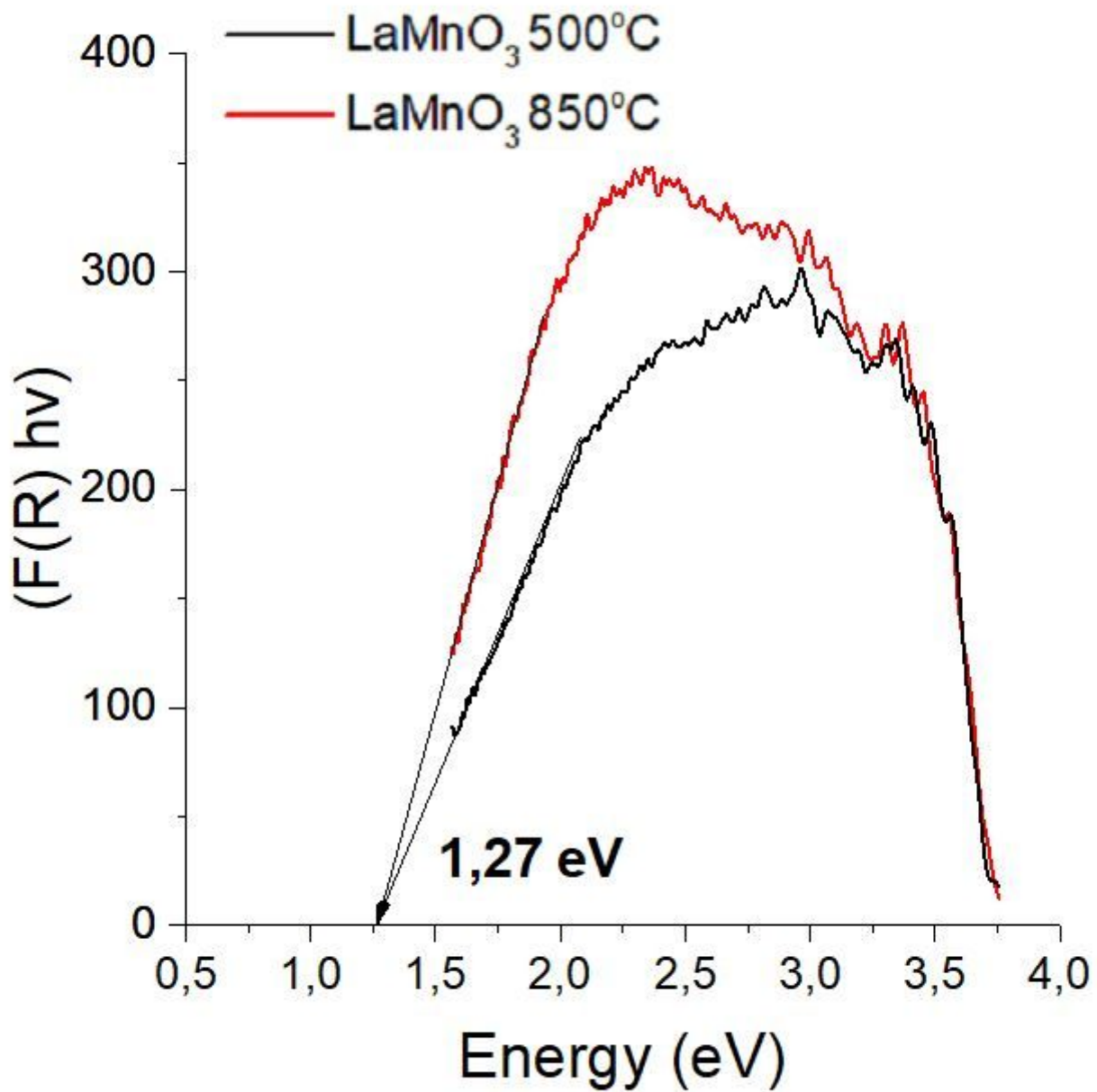


Figure 14

The bandgap energy $((F(R) \cdot hv)^2$ vs. hv) plots of LaMnO_3 powders annealed at 500°C and 850°C

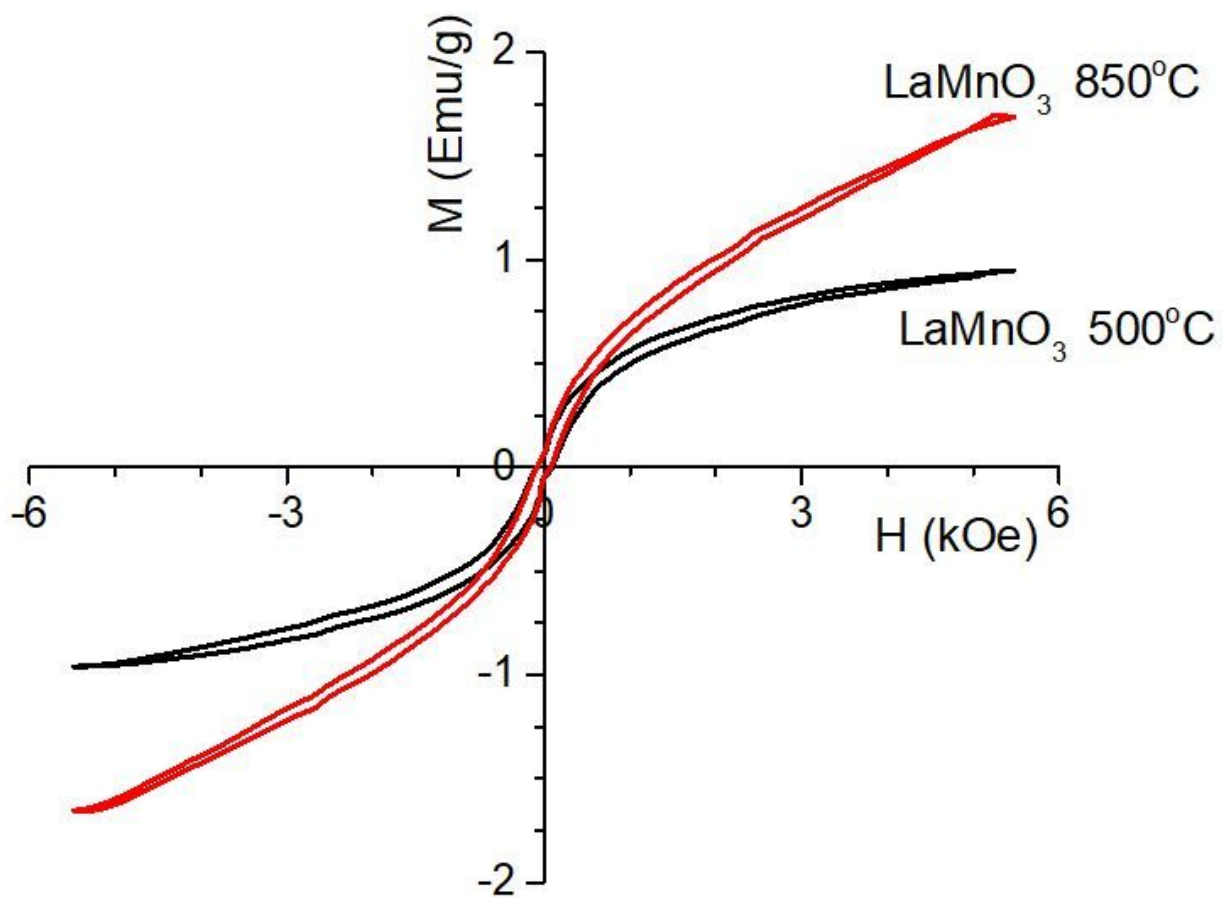


Figure 15

VSM results of LaMnO_3 powders annealed at 500°C and 850°C .